



HAL
open science

Multiscale Observations of Deep Convection in the Northwestern Mediterranean Sea during Winter 2012-2013 Using Multiple Platforms

Pierre Testor, Anthony Bosse, Loïc Houpert, Félix Margirier, Laurent Mortier,
Hervé Le Goff, Denis Dausse, Matthieu Labaste, Johannes Karstensen, Daniel
Hayes, et al.

► **To cite this version:**

Pierre Testor, Anthony Bosse, Loïc Houpert, Félix Margirier, Laurent Mortier, et al.. Multiscale Observations of Deep Convection in the Northwestern Mediterranean Sea during Winter 2012-2013 Using Multiple Platforms. *Journal of Geophysical Research. Oceans*, 2018, 123 (3), pp.1745-1776. 10.1002/2016JC012671 . hal-01764125

HAL Id: hal-01764125

<https://univ-perp.hal.science/hal-01764125v1>

Submitted on 9 Dec 2020

HAL is a multi-disciplinary open access archive for the deposit and dissemination of scientific research documents, whether they are published or not. The documents may come from teaching and research institutions in France or abroad, or from public or private research centers.

L'archive ouverte pluridisciplinaire **HAL**, est destinée au dépôt et à la diffusion de documents scientifiques de niveau recherche, publiés ou non, émanant des établissements d'enseignement et de recherche français ou étrangers, des laboratoires publics ou privés.

1 Multi-scale observations of deep convection in the
2 northwestern Mediterranean Sea during winter
3 2012-2013 using multiple platforms

Pierre Testor¹, Anthony Bosse², Loïc Houpert³, Félix Margirier¹, Laurent Mortier⁴, Hervé Legoff¹, Denis Dausse¹, Matthieu Labaste¹, Johannes Karstensen⁵, Daniel Hayes⁶, Antonio Olita⁷, Alberto Ribotti⁷, Katrin Schroeder⁸, Jacopo Chiggiato⁸, Reiner Onken⁹, Emma Heslop¹⁰, Baptiste Mourre¹⁰, Fabrizio D’Ortenzio¹¹, Nicolas Mayot¹¹, H loise Lavigne¹¹, Orens de Fommervault^{11,12}, Laurent Coppola¹¹, Louis Prieur¹¹, Vincent Taillandier¹¹, Xavier Durrieu de Madron¹³, Francois Bourrin¹³, Gael Many¹³, Pierre Damien¹⁴, Claude Estournel¹⁴, Patrick Marsaleix¹⁴, Isabelle Taupier-Letage¹⁵, Patrick Raimbault¹⁵, Robin Waldman¹⁶, Marie-Noelle Bouin^{16,17}, Herv  Giordani¹⁶, Guy Caniaux¹⁶, Samuel Somot¹⁶, V ronique Ducrocq¹⁶, Pascal Conan¹⁸.

Corresponding author: P. Testor, Laboratoire d’Oc anographie et de Climatologie: Exp rimentation et Approches Num riques (LOCEAN), Universit  Pierre et Marie Curie, 4 place Jussieu, 75252 Paris cedex 05, France (testor@locean-ipsl.upmc.fr)

¹CNRS-Sorbonne Universit s (UPMC)

4 **Abstract.** During winter 2012-2013, open-ocean deep convection which
5 is a major driver for the thermohaline circulation and ventilation of the ocean,
6 occurred in the Gulf of Lions (Northwestern Mediterranean Sea) and has been
7 thoroughly documented thanks in particular to the deployment of several glid-
8 ers, Argo profiling floats, several dedicated ship cruises, and a mooring ar-
9 ray during a period of about a year.

10 Thanks to these intense observational efforts, we show that deep convec-
11 tion reached the bottom in winter early in February 2013 in a area of max-
12 imum $28 \pm 3 \text{ } 10^9 \text{ m}^2$. We present new quantitative results with estimates of
13 heat and salt content at the sub-basin scale at different time scales (on the
14 seasonal scale to a ten days basis) through optimal interpolation techniques,
15 and robust estimates of the deep water formation rate of $2.0 \pm 0.2 Sv$. We pro-
16 vide an overview of the spatio-temporal coverage that has been reached through-
17 out the seasons this year and we highlight some results based on data anal-
18 ysis and numerical modeling that are presented in this special issue. They
19 concern key circulation features for the deep convection and the subsequent
20 bloom such as Submesoscale Coherent Vortices (SCVs), the plumes and sym-
21 metric instability at the edge of the deep convection area.

Univ. Pierre et Marie Curie, Paris

1. Introduction

22 Open-ocean deep convection is a key process that materially exchanges heat and salt, as
23 well as momentum, between the surface layers and the deep ocean in localized regions of
24 the global ocean and is a major contributor to the thermohaline circulation [*Marshall and*
25 *Schott, 1999*]. Open-ocean deep convection happens in winter and results in oceanic deep
26 water formation. The Mediterranean Sea, the Weddell Sea, the Labrador Sea and the
27 Greenland Sea are deep convection areas that are relatively well documented but many
28 details about what is occurring during the different phases of convection and what drives
29 the vernal bloom that can be observed during the restratification phase are still unclear
30 because many scales appear to interplay and the vertical dimension is difficult to observe.

31

32 Deep convection in the Gulf of Lion was first described by the *MEDOC-Group* [1970]
33 in three phases:

34 • the preconditioning of the area by a cyclonic gyre circulation in the whole northwest-
35 ern Mediterranean Sea producing a doming of isopycnals toward the surface centered at
36 about (42°N, 5°E), exposing a large body of weakly stratified waters to local cooling and
37 evaporation, due to dry and cold Mistral and Tramontane winds blowing over the Gulf of
38 Lion;

39 • the vertical mixing due to buoyancy loss generated by intense surface cooling and
40 evaporation reaching about 1000 W/m² for short periods and allowing overturning of the
41 water column;

06)-CNRS-IRD-MNHN, UMR 7159,

42 • the spreading/restratification phase with newly-formed deep waters propagating
43 away from the formation site while stratified waters around invade the deep convection
44 area.

45 This framework is still commonly used in all studies concerning deep convection pro-
46 cesses, in all locations of deep water formation, likely because it clearly depicts the major
47 physical drivers. Furthermore, it is well-known winter mixing, and in particular deep con-
48 vection, participates to transfers of biogeochemical properties like oxygen, all inorganic
49 and organic, dissolved and particulate, matters and is a major contributor to the func-
50 tioning of the upper-ocean ecosystem by supplying in particular nutrients from the deep
51 ocean to the euphotic layer. Convection is one of the major drivers of the phytoplankton
52 phenology [*Lavigne et al.*, 2013] as well as of the deep pelagic and benthic ecosystems
53 [*Pusceddu et al.*, 2010; *Stabholz et al.*, 2013; *Tamburini et al.*, 2013]. Satellite ocean color
54 images show high phytoplankton abundances at the surface, starting and increasing dur-
55 ing the violent mixing periods around a 'blue hole' where deep mixing occurs and then
56 at the sub-basin scale during restratification events, generally in April. This is the onset
57 of the most intense bloom in the Mediterranean Sea. As such, it appears to be a major
58 phenomenon for the evolution of the Mediterranean Sea that contributes to the evolution
59 of this physical-biological system, which is considered as a hot spot for biodiversity and
60 climate change [*Giorgi*, 2006; *Coll et al.*, 2010]. The northwestern Mediterranean Sea is
61 well-known to be subject to rapid and drastic responses to climate change [*Cacho et al.*,
62 2002; *Somot et al.*, 2006], and it is today of the ultimate importance to better understand

Laboratoire d'Océanographie et de

63 the response of the Mediterranean water cycle [*Adloff et al.*, 2015] and marine ecosystems
64 to external constraints [*Herrmann et al.*, 2013, 2014; *Auger et al.*, 2014].

65 From a biogeochemical perspective, the Mediterranean has long been known as an oligo-
66 trophic area with relatively low nutrient concentrations, characterized by a general West
67 to East gradient of increasing oligotrophy. The elemental stoichiometry in all compart-
68 ments (i.e. particulate and dissolved inorganic and organic) reveals an excess of carbon,
69 a deficiency in phosphorus relative to nitrogen and a sporadic silicate deficiency [*Béthoux*
70 *et al.*, 2002] as compared to other oceanic provinces. It is well known that the elemen-
71 tal composition of biotic and abiotic compartments can widely vary with environmental
72 conditions (light, temperature, trophic status), or growth rate of living organisms [*Conan*
73 *et al.*, 2007], but the Mediterranean anomalies, though frequently explored, still represent
74 open issues for the understanding of the functioning of the marine ecosystem in gen-
75 eral. Macro-nutrient concentrations there depend on the exchanges through the Straits
76 of Gibraltar and Bosphorus, atmospheric depositions, and river discharges, whereas their
77 distributions are controlled by both physical (i.e. dense water formation) and biological
78 activities (consumption/mineralization). Continental inputs are characterized by a strong
79 variability in terms of quantity and quality, dominated by extreme events (i.e. large river
80 floods and dust deposits), due to the climatic specificity of this region. These inputs, lat-
81 eral fluxes and the exchanges between the surface and deep layers across the nutriclines,
82 are dominant processes for the development of phytoplankton and higher trophic levels.

83 From a physical point of view, the violent atmospheric forcing events that trigger deep
84 convection in the center of the preconditioned area [*Somot et al.*, 2016; *Herrmann and*

Climatologie (LOCEAN), Institut Pierre

85 *Somot*, 2008] produce a *Mixed Patch* that is unstable. Many studies have shown the
86 important role of baroclinic instability for deep convection [*Killworth*, 1976; *Gascard*,
87 1978; *Killworth*, 1979; *Legg and Marshall*, 1993; *Visbeck et al.*, 1996; *Jones and Marshall*,
88 1997; *Legg et al.*, 1998; *Testor and Gascard*, 2006] because it is a mechanism that could
89 occur throughout the deep convection process, from the preconditioning to the spreading
90 phase, that can contribute to vertical mixing by inducing vertical velocities order of 1-
91 100m/day over periods of days, as well as to lateral fluxes by eddy shedding. At a later
92 stage, once the atmospheric forcing had considerably lessened, the *Mixed Patch* becomes
93 highly unstable and there is a general breakup on a time scale of a few weeks [*Madec*
94 *et al.*, 1991]. Many observations of Submesoscale Coherent Vortices (SCVs as introduced
95 by *McWilliams* [1985]) of a scale $O(5\text{km})$ composed of newly-formed waters [*Lilly et al.*,
96 1999; *Gascard et al.*, 2002; *Testor and Gascard*, 2003, 2006] document the eddy field in
97 such areas and this scale likely modulates the variability in the vicinity of the *Mixed*
98 *Patch* presenting a horizontal scale of $O(100\text{km})$. All these SCVs appear to have similar
99 characteristics (small radius, large aspect ratio and long lifetime of the order of a year).
100 They are involved in the large scale circulation of the newly formed deep waters (spreading
101 phase) and contribute to the deep ventilation. It appears these vortices are numerous,
102 can travel 100s of km during their lifetime and can export waters composing their cores
103 over long distances and periods of time.

104 In the *Mixed Patch*, intense vertical velocities $O(10 \text{ cm s}^{-1})$ were observed in cells with
105 horizontal and vertical scales of $O(1 \text{ km})$ [*Schott and Leaman*, 1991; *Schott et al.*, 1996]
106 at a smaller scale than the observed eddies. Supported by numerical modeling and tank

Simon Laplace (IPSL), Observatoire Ecce

107 experiments [Marshall and Schott, 1999] could explain these so-called *plumes* resulting
108 from hydrostatic instability and earth rotation. The *Mixed Patch* would result from an
109 integral effect of these non-penetrative *plumes* [Send and Marshall, 1995] balanced by
110 lateral buoyancy fluxes. However, these experiments considered a homogeneous ocean
111 forced by a heterogeneous atmosphere (disc-shaped atmospheric forcing) and did not
112 account for preconditioning effects at large, meso- or even submeso- scales. On the other
113 hand, Legg and McWilliams [2001] proposed that the homogenization of the newly formed
114 deep waters was likely due to the turbulent geostrophic eddy field, and eddies presenting
115 a doming of isopycnals toward the surface could definitely act as local preconditioners
116 favoring locally deep convection.

117 It is clear that physical and biogeochemical processes act in setting up the Spring bloom
118 that is observed after deep convection events. Vertical and horizontal fluxes of particulate
119 and dissolved inorganic and organic matters are constrained by physical processes and
120 biogeochemical cycles. However, little is known of the scales at which these processes
121 interact and most of the questions that are still unresolved concerning Mediterranean
122 biogeochemical evolution deal with the temporal variability of the key processes that
123 govern the functioning and budgets of the different physical, chemical, and biological
124 compartments.

125 Observational limits are the principal causes of this uncertainty. The preconditioning,
126 violent mixing and restratification/spreading phases do overlap with a preconditioning
127 phase starting at least the previous Summer and a spreading phase extending possibly
128 over years, while presenting high-frequency variability. The *Mixed Patch* extends over

Terra, 4 place Jussieu, F-75005 Paris,

129 100 km with modulations at (sub)mesoscale $O(5\text{ km})$ and small scale $O(1\text{ km})$ while
130 the bloom seems to extend over the whole northwestern basin with high variability at
131 meso/submeso/small scale, often clearly coupled to the physical one. According to [*Dur-*
132 *rieu de Madron et al., 2011*], bloom and deep convection events result from an 'history'
133 of at least 6-8 months beforehand that needs to be characterized. This observational
134 challenge motivated a multi-platform experiment aiming at a continuous description of
135 the water column at the basin/meso/submeso scales over a year. Building on long-term
136 observational efforts in that area, additional observations were carried out in 2012-2013
137 to try to achieve this goal.

138 In the present paper, we will describe and analyze the results obtained from this 2012-
139 2013 DEWEX (DEnse Water EXperiment) experiment coordinating different projects in
140 that area, providing a more complete and extended description of the different phases of
141 deep convection. We will first describe the sampling strategy of the experiment and the
142 area under study, based on all in situ potential temperature, salinity, potential density,
143 and fluorescence of chl-a profiles as well as currents and depth-average currents estimates
144 that were collected in this framework thanks to ships, gliders, moorings, profiling floats
145 and surface drifters. We will provide an overview of the spatio-temporal coverage that
146 was achieved during this experiment, describe the evolution of the northwestern Mediter-
147 ranean Sea mainly from a physical point of view, and estimate newly-formed deep water
148 formation rates and energy fluxes. We will finally discuss the importance of different phys-
149 ical processes for the deep convection and subsequent bloom, that were observed during

France

150 our study period based on different studies developed in this framework, before a general
151 conclusion.

2. The multi-platform sampling strategy

152 Taking advantage of long-term observational efforts (Long-term Observation Period,
153 LOP) carried out in the framework of MOOSE (Mediterranean Ocean Observing System
154 for the Environment, <http://www.moose-network.fr>) in this region, additional observa-
155 tions (Enhanced Observation Period, EOP and Special Observation Periods, SOPs) were
156 carried out in the northwestern Mediterranean Sea to try to achieve the above-mentioned
157 goal, thanks to several European and national projects (see Acknowledgments). Thanks to
158 numerous research cruises, gliders, profiling floats, moorings and drifters, a very significant
159 number of oceanic vertical profiles, could be collected to reach a better characterization
160 of deep convection in this region, and the subsequent bloom.

161 The approach was to combine the sampling capabilities of R/Vs with autonomous plat-
162 forms to reach an adequate spatio-temporal coverage during a period starting in Summer
163 to the next, and to be able to capture all the key processes involved in deep convection
164 during a year. Our "study period" was July 1st, 2012 to October 1st, 2013 and the data
165 considered here includes gliders, ship CTD, profiling floats, drifters, and moorings. All
166 data considered are displayed on Figure 1 together with the temporal sampling strategy
167 for each platform.

²Geophysical Institute, University of

168 Figure 2 describes typical ocean color satellite images that were obtained, when the
169 sky was clear, and illustrates the different phases of deep convection. Summer-Fall is a
170 period of low phytoplankton abundance followed by a Winter period during which high
171 phytoplankton abundance can be observed around a 'blue hole' in the deep convection
172 area and then, a Spring period dominated by a planktonic bloom covering the entire
173 northwestern basin until it fades away in late Spring.

174 To really understand and assess the deep convection and bloom processes, a vertical
175 description of the variations that can be observed with satellites was required and an
176 optimal combination of the various in-situ platform sampling capabilities has been sought.
177 The observational efforts required:

- 178 • periods of intensive observation at certain key moments (SOPs), allowing access to
179 a full annual cycle for the entire zone. It is indeed essential to monitor the evolution of
180 the ocean in the study area over specific periods of the year, so changes related to dense
181 water formation can be assessed for both water balances and elements involved in the
182 functioning of the ecosystem and the sequestration of matter;
- 183 • a sampling strategy compatible with the large, meso- and submeso- scale phenomena
184 and which can be used effectively to constrain modeling studies. ;
- 185 • a coordination with periods of intensive atmospheric observations of intense events;
- 186 • a consistency with observations carried out on the long-term in the area.

187 Different models were used in this program in combination with the observational efforts
188 presenting different configurations (and in particular horizontal resolution) depending

Bergen and Bjerknes Center for Climate

189 on the different processes under focus (large/small space/time scales) and the sampling
190 strategy was designed to provide validation (and initialization) at the sub-basin scale as
191 well as at submesoscale taking advantage of the different sampling capabilities of the
192 platforms considered here.

193 Ship cruises were planned before, during, and after deep convection and bloom events,
194 while gliders, profiling floats, moorings (at few locations) and drifters could provide infor-
195 mation in-between. Even if this information is more limited in terms of observed variables,
196 most of the autonomous platforms deployed during the study period were equipped with
197 physical (temperature, salinity, currents) and bio-optical (dissolved oxygen, chl-a fluores-
198 cence, turbidity, CDOM, nitrates) sensors and this allows a quasi-continuous description
199 of the physical forcing on key biogeochemical variables.

200 Research cruises mainly intended to provide a CTD network covering the whole sub-
201 basin at different periods of the year. The CTD casts were mainly carried out at relatively
202 low horizontal resolution (about 20nm except on the continental slope where the distance
203 between the CTD casts was lower in order to sample the boundary circulation) to cover
204 the whole sub-basin in about 3 weeks.

205 For gliders, the planned sections were designed with a low repeat rate but large spatial
206 coverage before and after deep convection events, while repeat-sections at higher repeat
207 rate (but smaller spatial coverage) were carried out during the "deep convection" period.
208 During this period, the plan was to make the gliders turn back along their planned repeat
209 sections as soon as the gliders were more than about 20km away from the deep convection
210 region.

Research, Bergen, Norway

211 Profiling floats were primarily deployed in the deep convection area just before, during,
212 and just after the violent mixing events. The aim was to document the evolution of the
213 *Mixed Patch* and to follow its break-up from a quasi-Lagrangian point of view, on even
214 longer timescales.

215 Drifting buoys were deployed north of the deep convection area and in the deep convec-
216 tion area before, during and after the violent mixing events. The aim was to document
217 the surface temperature and salinity, and the atmospheric parameters during the period
218 of strong surface heat loss.

219 One overarching objective with a massive deployment of autonomous platforms was
220 to carry out about 40/300 profiles on average per day/week, distributed over the whole
221 northwestern Mediterranean Sea, at any time during the whole deep convection/bloom
222 period (including preconditioning and spreading/restratification phases) to adequately
223 document the water column evolution.

3. Data

3.1. Ship CTD data

224 Several, and often basin scale, cruises were carried out in the northwestern Mediter-
225 ranean Sea during our study period (see table 1). Since 2010, each of the MOOSE-GE
226 cruise, on board *R/V Thetys II* or *R/V Le Suroît*, provides a yearly snapshot in summer
227 of the open-ocean part of the basin with about 70–100 CTD stations distributed on a
228 star-shape array centered on the deep convection zone with branches about perpendic-

³Scottish Association for Marine Science,

229 ular to the continental slope around. A major objective of the MOOSE observatory is
230 to monitor the deep waters formation in the Gulf of Lions and to be able to detect and
231 identify long-term environmental trends and anomalies of the marine environment and
232 ecosystem in response to climate change. The remnants of the convective events happen-
233 ing in February are observed at the basin scale and this allows to monitor the deep water
234 formation rate as for instance demonstrated by *Waldman et al.* [2016].

235 The DEWEX and DOWEX cruises, on board *R/V Le Suroît* and *R/V Tethys II* respec-
236 tively, followed the same spatial sampling strategy and intended to cover the seasonal cycle
237 with a focus first on the Winter-Spring period when deep convection and bloom occurs
238 and second, in September for the preconditioning. They provided very accurate profile
239 measurements every 20nm or so, covering the whole basin. CTD casts have also been
240 collected during the HyMeX SOP1 cruises (see [*Ducrocq et al.*, 2014; *Lebeaupin-Brossier*
241 *et al.*, 2014]) from *R/V Urania* and *R/V Le Provence*, and during the HyMeX SOP2
242 cruises from *R/V Tethys II* and *R/V Le Provence*. To span the preconditioning period,
243 Marisonde and Surface Velocity Program (SVP) drifters were launched from a dedicated
244 cruise early September 2012, on a transect off Toulon (5°E). To deploy Argo floats in
245 the Mixed Patch, and re-position the Marisonde buoys for the convection period, support
246 cruises were set-up late January and late February 2013. In order to catch an intense
247 Mistral wind event and its impact on the convection, *R/V Le Provence* was chartered to
248 enable sampling on alert [*Estournel et al.*, 2016a]. In total, about 400 CTD casts were
249 carried out during our study period.

Oban, Argyll, Scotland.

250 The ship CTD data are displayed on Figure 3. This is the reference data set and it
251 describes well the different water masses that are present in the area during our study
252 period. Because of the number of casts (among the highest numbers of CTD casts ever
253 carried out in a year in this area) we certainly have a nice statistical description of all
254 kind of profiles that can be observed, having in mind a water mass classification. One can
255 identify the Atlantic Water (AW) characterized by a minimum in salinity and its modal
256 form, the Winter Intermediate Water (WIW), the Levantine Intermediate Water (LIW)
257 below, characterized by a maximum in salinity and in potential temperature, and the
258 Western Mediterranean Deep Waters (WMDW) and the newly-formed Western Mediter-
259 ranean Deep Waters (nWMDW) generally at greater depths, that are characterized by a
260 potential temperature of 12.91-12.94°C and a salinity of 38.45-38.48, the highest values
261 being typical of the newly formed waters and reciprocally, the lowest ones being typical of
262 water formed previously. Figure 3a shows the profiles collected before the deep convection
263 events with a narrow distribution around an almost linear relationship between the deep
264 and intermediates waters. A white dot indicates the presence of nWMDW formed the
265 previous year that cohabits with even older ones. During the winter mixing events (Fig-
266 ure 3b) the distribution of Θ -S values is more scattered (with lower probabilities) with a
267 number of accumulation points often saltier than before. After a period of mixing, a sig-
268 nificant volume of newly formed deep water emerges (around the white dot on Figure 3c).
269 Note that this year, cascading was relatively weak compared to intense cascading events
270 that can be observed every 6 years or so, as shown by [*Durrieu de Madron et al., 2013*]

⁴ENSTA-Paristech, Laboratoire

271 or [Houpert *et al.*, 2016]. Deep water formed by cascading apparently did not propagate
272 very deep in 2012-2013. Such a water mass has been detected, as shown by glider sections
273 crossing the continental shelf and slope along Cape Creus canyon and at the surface with
274 the TRANSMED thermosalinometer ([Taupier-Letage *et al.*, 2016]), but is not visible on
275 the Θ -S diagrams presented on Figure 3 and is not considered as a major newly-formed
276 deep water mass during this winter.

3.2. The mooring lines data

277 The LION mooring line is in the vicinity of the center of the deep water formation zone
278 at $42^{\circ}02'N/4^{\circ}41'E$ (bottom depth at 2350m, see Figure 1). It was equipped for the study
279 period with eleven SeaBird Microcats SBE37 (conductivity-temperature-pressure sensor),
280 ten RBR temperature sensors, and five Nortek Aquadopp current meters measuring hori-
281 zontal and vertical currents, spaced along the line from 150 m to 2300 m. The DYFAMED
282 mooring line in the Ligurian Sea at $43^{\circ}25'E/7^{\circ}54'N$ was equipped similarly but with fewer
283 instruments (four SeaBird Microcats SBE37 at about 200 m, 700 m, 1000 m and 2000 m,
284 Nortek Aquadopp current meters at 100 m and 1000 m). These moorings provide rela-
285 tively profiles with low resolution along the vertical of the water column but about every
286 30 minutes, this rate being the lowest sampling rate of all instruments attached to the
287 lines.

288 The LION and AZUR Météo-France moored buoys are located at about $42^{\circ}06'N/4^{\circ}38'E$
289 and $43^{\circ}23'N/7^{\circ}50'E$ close to LION and DYFAMED mooring lines, respectively. They
290 provided hourly measurements of atmospheric parameters (atmospheric pressure, tem-

d'Océanographie et de Climatologie

291 perature, relative humidity, wind speed and direction, downward radiative fluxes) and
292 surface oceanic parameters from a SeaBird Microcat SBE37 during our study period.
293 Additionally, at the LION surface buoy, twenty NKE Instrumentation SP2T sensors pro-
294 vided hourly measurements of pressure and temperature from the surface down to 250 m
295 to complement water column measurements carried out between 150m and the bottom
296 by the LION mooring line [*Bouin and Rolland, 2011*]. Note that no surface turbulent
297 heat (sensible and latent) and momentum flux measurement was carried out. Fluxes
298 were estimated in this study from surface parameters through the use of turbulent flux
299 parameterization from *Fairall et al. [2003]*.

300 The LACAZE-DUTHIERS and PLANIER moorings, at about 42°25'N/3°32'E and
301 43°01'N/4°48'E respectively, were equipped with CTD sensors (Microcats) and cur-
302 rentmeters at 500 m and 1000 m depths. Like DYFAMED and LION/LIONCEAU
303 (42°01'N/4°48'E), these two moorings are also equipped with sediment traps to moni-
304 tor the fluxes through the canyons but only hydrographical data from these moorings are
305 used in this study.

3.3. Profiling floats data

306 Profiling floats drift autonomously at a given parking depth for a given time period,
307 typically 1-10 days. At the end of their drifting time, they dive to 2000m depth (or
308 sometimes 1000m depth) and collect a profile of temperature and salinity subsequent
309 ascent to the surface. The collected data are sent in real-time to a data center before
310 the floats return to their parking depth. During our study period, 27 floats deployed in

(LOCEAN), Palaiseau, France.

311 the framework of Argo and MedArgo and Bio-ArgoMed, were active in this area. Due
312 to the Mediterranean specificity, the MedArgo program has set the interval between the
313 successive surfacing of Argo floats to be 4-5 days and their parking depth to $\sim 400\text{m}$,
314 the approximate depth of the LIW. During our study period, other float configurations
315 provided different results such as casts down to 1000m depth every day with parking
316 depths at 1000 m depth for some period of time or casts to 2000m depth every 5 days
317 etc. For instance, bio-optical floats were configured to profile everyday when drifting in
318 the *Mixed Patch* to better observe it and then, when atmospheric fluxes reverted, were
319 remotely reconfigured to cycles of 5 days to document at a larger scale the spreading of
320 the newly-formed deep waters. Profiling floats collected a total of about 2700 potential
321 temperature and salinity profiles in the northwestern Mediterranean Sea during our study
322 period. Many were equipped with oxygen sensors [*Coppola et al.*, 2017] and others with
323 nitrate, fluorescence of Chl-a, fluorescence of CDOM, and turbidity sensors [*Mayot et al.*,
324 2017] to document the ventilation processes and the physical-biogeochemical interactions.

3.4. Drifter data

325 Two types of drifting buoys were deployed during the HyMeX SOP1-SOP2 periods.
326 SVP drifters provide measurements of atmospheric pressure, SST and SSS (SVP-BS type
327 drifters) or water temperature from the surface down to 80 m (SVP-BTC drifters). They
328 are attached to a 15-m drogue and follow the surface currents. Five salinity SVP drifters
329 and five temperature SVP drifters were deployed before the deep convection period in

⁵GEOMAR, Kiel, Germany.

330 the north of the Gulf of Lions. They provided a good coverage of the deep convection
331 area before and during the mixing period. Marisonde buoys are particular drifters that
332 measure the water temperature from the surface down to 250 m. In addition, they record
333 atmospheric pressure, temperature and wind. They are however more sensitive to the
334 surface wind than to the current and cannot be considered as Lagrangian. Five of them
335 were dropped in the north of the deep convection area at the beginning of September 2012,
336 five more at the same place in February 2013 during the HyMeX SOP 1 and 2 cruises.

3.5. Gliders data

337 Gliders [*Testor et al.*, 2010] are steerable autonomous platforms that sample the ocean
338 along saw-tooth trajectories between the surface and a maximum depth of 1000 m today.
339 As the slopes of isopycnals (a few degrees) are generally much smaller than the pitch
340 angle of the glider (about $\pm 15\text{-}30^\circ$), the glider dives and ascents can be considered as
341 vertical profiles to a large extent. Under this assumption, two consecutive profiles down
342 to 1000 m are separated by approximately 2–4 km and 2–4 h depending on the currents
343 and the sampling strategy of the platform, with sensors being powered on during dives
344 and/or ascents. With a horizontal speed of 30–40 km day⁻¹ relative to the water, gliders
345 are perfectly suited to capture balanced circulation features and eddies that propagate
346 more slowly. By comparing dead reckoning navigation and GPS fixes at the surface,
347 gliders can also deduce a depth-average current between two surfacing. The average of
348 the currents over a dive provides a transport estimate, being close to a measure of the

⁶Oceanography Center, University of

349 average currents between surfacing (generally 2-4 km apart) and between the surface and
350 the depth achieved (generally 1000m depth). The gliders used during this experiment were
351 equipped with the same sensors as for the profiling floats for measurements of potential
352 temperature, salinity, but also oxygen concentration, fluorescence of Chl-a, fluorescence
353 of CDOM, and turbidity. They provided about 40 000 profiles over our study period.

4. Data harmonization and integration

4.1. Temperature and Salinity estimates

354 Two coupled Seabird SBE 911+ CTD were used during MOOSE-GE/DOWEX/DEWEX
355 cruises with pre- and post- calibrations from the manufacturer. The data have also been
356 compared to the analysis of the Rosette water samples with a Guideline Autosol. The
357 absolute accuracy of this calibration method is estimated to be about 0.005 for the salin-
358 ity, and 0.001°C for the temperature. These calibrated CTD casts provide a ground truth
359 used for the calibration of other instruments such as the deep mooring lines (LION and
360 DYFAMED in particular) and the data collected by autonomous gliders, profiling floats
361 through alignments on a linear T/S relationship observed at depths (700-1000m) each
362 year at the basin scale, and point-to-point intercomparison exercises.

363 An intercalibration of the instruments on the LION and DYFAMED mooring lines
364 after and before each deployment has been carried out to ensure the consistency of the
365 mooring sensors with the ship CTD dataset. Each year, during the mooring maintenance
366 operations, microcats are attached to the Rosette and a cast consisting in a 20 minutes
367 stop at 1000m depth is carried out with all the instruments. A relative calibration of the

Cyprus, Nicosia, Cyprus.

368 moored instruments with each other and relative to the shipborne CTD probe SBE 911+
369 is performed as in [Testor et al., 2016].

370 Each glider is equipped with a pumped or unpumped CTD sensor that generally needs
371 to be corrected with an offset as a first order correction for each deployment. By compar-
372 ing the gliders data in the deep layers (700–1000 m) with nearby calibrated CTD casts
373 collected by R/V (<15 km and <3 days), and/or with the calibrated data of the mooring
374 lines LION and DYFAMED (<2.5 km and <18 h, about the inertial period in this region),
375 we checked the consistencies of the hydrographical data in the deeper layers sampled by
376 the gliders, as the variability of the temperature and salinity are relatively small at those
377 depths [Bosse et al., 2015, 2016]. The deduced offsets that are applied are on average of
378 about 0.01°C and 0.01 in Potential Temperature and Salinity respectively. In addition,
379 the method of Garau et al. [2011] was used to correct thermal lag issues of the gliders
380 pumped and unpumped CTD probes. Note this applies second order corrections every-
381 where but in sharp summer thermoclines (order of 1-10°C over less than 10 m) where
382 salinity measurements can indeed be affected. If no direct comparison with calibrated
383 data is possible ($\sim 30\%$ of the deployments), only salinity is offset to fit the linear θ - S
384 relationship holding between the intermediate and deep layers (700–1000 m) and provided
385 by the calibrated data from R/V (see figure 3). Glider time series have been sliced in up-
386 and down-casts and interpolated every 1 m along the vertical to provide equivalents of
387 vertical profiles located at average up- or down- casts times and locations.

⁷Consiglio Nazionale delle Ricerche -

388 We applied similar calibration procedures for the Argo profiling floats and drifters
389 equipped with thermistor chains below, as for the gliders. The thermal lag issue is a
390 known problem for profiling floats too (gliders are equipped with the same probes) but
391 when vertical resolution is not high enough to resolve the thermocline (and this is often
392 the case for profiling floats not configured to resolve sharp thermoclines), no thermal lag
393 correction could be applied and a vertical interpolation just applied. No correction was
394 applied on drifters thermistor chain data, timeseries data being just interpolated along
395 the vertical on a 1m basis, like mooring data, to estimate profiles.

396 This method ensures the autonomous platforms CTD errors in temperature and salinity
397 to overall be smaller than respectively 0.01°C and 0.01. On the other hand, the variability
398 in θ -S characteristics could be estimated with unique platforms at different levels based
399 on a water mass identification approach. As illustrated by Figure 4f, differences between
400 the nWMDW in 2013 and former WMDW at great depth are about 0.04°C in potential
401 temperature (and 0.03 in salinity, not shown). Similarly, the differences in potential
402 temperature and salinity between nWMDW and LIW (maxima of Potential Temperature
403 and Salinity) are about 0.3°C (Figure 4e) and 0.3 respectively, in the intermediate layers.
404 Finally, the differences between nWMDW and AW (minimum of Salinity) is about 0.4 in
405 salinity with a wide range of relatively similar temperatures at any time (prominence of
406 the seasonal cycle) in the open sea region (Figure 4d). Therefore the overall corrected
407 data set can be considered as consistent in accuracy for studying the evolution of the
408 water masses and the deep convection processes, with a reference to high-quality values
409 from ship measurements and water samples.

Istituto per l'ambiente marino costiero

4.2. Chl-a concentration estimates

410 During MOOSE-GE, DOWEX, and DEWEX cruises, Chlorophyll-a fluorometers cal-
411 ibrated by manufacturers were available on all kind of platforms (i.e. ships, gliders,
412 profiling floats). Moreover, water samples were filtered during ship surveys to estimate
413 Chlorophyll-a concentration through High Pressure Liquid Chromatography (HPLC) tech-
414 nique [*Gieskes et al.*, 1983]. The harmonization of the whole fluorescence data set was
415 carried out by using the *Lavigne et al.* [2012] technique, which provides fluorometer-specific
416 calibration coefficients (offset and slope) by comparison with ocean color satellite images.
417 Briefly (see *Lavigne et al.* [2012] for a complete explanation of the method), fluorescence
418 profiles are initially corrected for photochemical quenching [*Xing et al.*, 2012]; then an
419 offset is evaluated by imposing zero value at depth below the Mixed Layer. Satellite
420 match-ups were then generated (+/- 4 hours temporal difference with satellite overpass,
421 using daily MODIS level 3, at 4 km spatial resolution products) and used to calculate
422 slope coefficients. Slope and offset coefficients were first evaluated on a single profile
423 basis. Then, to keep the high spatio-temporal variability measured by autonomous plat-
424 forms, a single coefficient was defined for each platform (for floats), for each deployment
425 (for gliders) or for each leg (for ships), by using median values. A visual check of the time-
426 series of the slope and off-set coefficients allowed to verify there was no significant drift in
427 fluorometer during float or glider missions or ship legs. When available (i.e. for most of
428 the ship fluorescence profiles, and on some autonomous platforms), a direct comparison of
429 the satellite-calibrated fluorescence with HPLC Chlorophyll estimations was carried out
430 (not shown). The median error is of 28%, indicating a general good performance of the

(CNR-IAMC) Oristano, Italy.

431 harmonization method applied here. Note that an enhanced calibration of the available
432 fluorometers was provided by *Mayot et al.* [2017], who opted for an improved calibration
433 (by directly comparing fluorometers data with HPLC), although a degraded data avail-
434 ability (only floats and ships having simultaneous HPLC samples at the float deployment
435 or during the ship surveys were used). *Mayot et al.* [2017] demonstrated, however, that
436 the satellite-derived calibration presented here is only slightly less accurate than their
437 enhanced method.

4.3. Depth-average current estimates

438 Calibrations of the compasses of the gliders have been performed before each deploy-
439 ment. The current estimates were corrected using estimates of the angle of attack from
440 the flight model used in *Margirier et al.*. Indeed, the typical angle of attack of a glider
441 is about 3° (during dives and opposite during ascents) and induces an artificial forward
442 oceanic current in the depth-average current estimates, if not taken into account. When
443 possible, the depth-average current estimates from gliders were compared to the mooring
444 current meters data (at 150 m and 1000m data) and the data were consistent for 1 cm s^{-1}
445 when both current meters data were strongly correlated and somewhat representative of
446 the 0–1000 m water column. Return points along trajectories allowed comparisons of
447 depth-average current estimates within few hours and km. Such a protocol ensures a rela-
448 tive accuracy of about 1 cm s^{-1} for both components of the estimates of the depth-average
449 currents, typically about the expected natural variability of depth-average currents over

⁸Consiglio Nazionale delle Ricerche -

450 such scales. This allows discarding the few data clearly having a compass bias over a
451 whole glider deployment (no deployment was discarded during our study period, but con-
452 sidering older data, it looks it is a quality control to apply). Outliers ($> 1 \text{ m s}^{-1}$) certainly
453 due to spurious and bad GPS fixes correspond to 0.1% of the data and were discarded
454 from our data set. In this study, we consider only 1000 m depth-average currents. This
455 includes currents in the open sea but also part of the boundary circulation which flows
456 roughly centered above the 1000 m isobath. It excludes depth-average current estimates
457 over shallower dives which are not directly comparable to depth-average current estimates
458 over 0–1000 m. The currents are generally more intense at the surface than at great depth
459 and depth-average currents estimated over shallower dives reflect the baroclinic compo-
460 nent in a different way. Keeping only depth-average currents estimates over 0-1000m
461 allows having a consistent data set for currents averaged along the vertical over this layer.

5. Objective analysis

462 Our objective analysis method consists in extrapolation in 2D along the horizontal
463 from several point observations distributed in space and time using a correlation function
464 [*Le Traon*, 1990]. At first order, one can consider a Gaussian correlation function describ-
465 ing fluctuations at given spatial and/or temporal scales L : $Cov(a, b) = E + S e^{-D(a,b)^2/L^2}$,
466 $D(a, b)$ being the temporal/spatial distance between two observations "a" and "b". S/E
467 is the signal over noise ratio. The error is considered small, about 10% of the estimated
468 variance of the signal.

Istituto di Scienze Marine (CNR-ISMAR),

469 To take into account the tendency of oceanic currents to follow f/H , f being the
 470 planetary vorticity and H the bottom depth, we can introduce an anisotropy as described
 471 in *Boehme and Send* [2005]. The covariance function considered is then: $Cov(a, b) =$
 472 $E + Se^{-D(a,b)^2/L^2 - F(a,b)^2/\Phi^2}$, $D(a, b)$ and $t(a, b)$ is the spatial distance, $F(a, b)$ is a distance
 473 in potential vorticity f/H defined as: $F(a, b) = |Q(a) - Q(b)|/\sqrt{Q(a)^2 + Q(b)^2}$ with $Q =$
 474 f/H . By taking $\Phi \simeq 0.1$, the ocean is relatively isotropic except in the continental slope
 475 areas where the data are clearly more correlated along-shore than cross-shore.

476 For a considered data set, these methods are used with respect to a large scale first guess
 477 constructed with all data collected over the seasonal cycle. The data are first binned on
 478 a grid of 10 km x 10 km on a monthly basis and then analyzed with a scale $L = 150$ km
 479 corresponding to the basin-scale gradients and relatively high errors of 70%. Then two
 480 further refinement steps are preceded. The first consists in an analysis at the mixed
 481 patch scale ($L = 75$ km) with the observations carried out in a ± 10 days period with a
 482 relative error of 60% in order to capture the large scale and intra-seasonal evolution of
 483 the mixed patch. Then a second step is performed using a smaller decorrelation scales
 484 ($L = 15$ km) and a smaller error of 10% in order to capture the mesoscale variability
 485 of the deep convection area. An analysis could be done every ten days from January to
 486 March at the basin-scale with a good data coverage thanks to the intense observational
 487 effort during that period. Analyses were performed for potential temperature, salinity,
 488 potential density and chl-a estimates over the whole domain with respect to related first
 489 guesses and the method provides geometrical error maps.

Venezia, Italy.

6. Results

6.1. Evolution of the deep convection area

490 Figure 4a shows time series of total heat fluxes characterized by a series of storm events
491 starting in September with important heat losses from the ocean about $400\text{-}800\text{ W/m}^2$.
492 The heat fluxes are consistently negative starting in November inducing a clear decrease in
493 surface temperature (Figure 4d) but no clear signal in surface salinity except in February
494 during which the salinity reaches a plateau of relatively high values (Figure 4c). The
495 cascading mentioned above can be observed on Figure 4b but it happens mid-February
496 after the mixing has reached the bottom offshore (figure 4g) and there is no signature at
497 1000m at Lacaze-Duthiers mooring (not shown).

498 Different time series of potential temperature from in-situ profile data are also shown
499 in Figure 4 (d, e, f), describing well the evolution of the deep convection area over the
500 water column, with respect to the boundary current region where advection dominates
501 (time series in grey).

502 Figure 4d and Figure 4e shows the evolution of the surface and intermediate waters
503 respectively. There is always a contrast in the potential temperature between the convec-
504 tion area and the boundary currents where water masses are advected and less modified
505 by vertical mixing processes. They also show the vertical propagation of the mixing, the
506 temperature averaged over the deepest layer reaching progressively the same values as
507 above.

⁹Helmholtz-Zentrum Geesthacht,

508 The Mixed Layer Depth (MLD) was estimated with the method of *Houpert et al.* [2016]
509 (see Figure 4g). These estimates show a slow deepening starting in October and a rapid
510 one starting late January (at about 1000m depth) before the mixing reaches the bottom
511 (mid February) and this is consistent with the time series of temperature above. It also
512 shows a period of deep mixing from the beginning to the end of February with a rapid
513 restratification at the beginning of March. The heat fluxes (see Figure 4a) are positive
514 for a short period of time before a second deep convection event triggered by a storm
515 Mid March. Deep convection reached the bottom again at that time. This second mixing
516 event is quite frequent when ones considers the deep convection from one year to another
517 [*Houpert, 2013*]. The short period of restratification allows to have very few buoyant
518 waters on-top of homogeneous ones and such stratification is easily eroded by a storm
519 during this period.

520 Changes in potential temperature in the deeper layers (see Figure 4f) occur at the
521 beginning of February. A CTD cast performed few hours after a storm confirmed the
522 winter mixing has reached the bottom by mid-February 2013. It raises sharply from
523 12.9 to 12.94 and then significant variations due to the presence of both WMDW and
524 nWMDW in the area converge slowly to 12.91 at the beginning of May. At this stage
525 old and newly-formed WMDW are relatively well mixed in the convection area and the
526 variability returns to a low level, similar as before the rapid rise, but a large volume of
527 water has increased in temperature and this corresponds to a significant heat storage.

528 The time series on Figure 4h and 4i illustrate how the phytoplankton responds to
529 the environment. The amount of estimated chl-a at the surface and on average seems to

Germany

530 increase mid-December when the MLD starts to present values greater than the base of the
531 euphotic layer at about 100m depth. At that time the winter mixing reaches waters that
532 are nutrient-rich and nutrients being brought to enlighten levels, this participates to the
533 growth of phytoplankton as shown in *D’Ortenzio et al.* [2014]; *Pasqueron de Fommervault*
534 *et al.* [2015]. When the mixing reaches depths greater than 1000m the surface chl-a drops
535 to lower values before a sharp increase mid-March during the restratification period. It
536 is likely the surface chl-a has dropped to low values again during the second deep mixing
537 event mid-March but unfortunately, very few platforms considered here were equipped
538 with a fluorometer at that time. However, enlarging the spatial domain (as in *Mayot*
539 *et al.* [2017]) the effects of the second event on the chlorophyll distribution could be
540 monitored. Surface chl-a values reach even greater values in April before a rapid decrease
541 in May once the system has stabilized and the nutrients being consumed in the euphotic
542 layer.

543 It is interesting to note that the low surface chl-a values observed before the restrat-
544 ification may result from dilution as the average chl-a over 0-300m (Figure 4i) presents
545 significant values of integrated chl-a compared to what can be estimated from the sur-
546 face only. In terms of productivity, the integrated chl-a concentration (reaching about
547 $100 \text{ mg}\cdot\text{m}^{-2}$) is about the same during the slow deepening of the mixed layer, the deep
548 convection violent events, or the planktonic bloom. The continuous (but slow) introduc-
549 tion of nutrients in the surface (mixed) layer during the fall contrasts with the rapid and
550 massive introduction of nutrients just after the deep mixing events. *Mayot et al.* [2017]

¹⁰SOCIB, Mallorca, Spain.

551 concluded that the spring bloom is more important than the autumnal one because of a
552 dilution effect during the mixed layer deepening. They concluded the higher net accumu-
553 lation rate of phytoplankton in spring in this region was not induced by a higher winter
554 replenishment of nitrate. The strong and long winter mixing could rather have induced
555 a change in zooplankton grazing pressure and silicate availability, leading to a stronger
556 phytoplankton spring bloom. Furthermore, a similar autumnal phytoplankton bloom (less
557 intense than the spring bloom) between bioregions might be ascribed to a mixing of the
558 summer deep chlorophyll maximum, to inputs of nutrients in the surface layer, and/or
559 also to photo-acclimation processes.

6.2. Energy fluxes

560 Thanks to the depth-average currents measured by the gliders, the evolution of the
561 energy content of the basin can also be described. Due to deep convection, newly-formed
562 deep waters form a volume of water denser than the surroundings. This increases the
563 potential energy of the system and is an energy reservoir that is then transformed into
564 kinetic energy, through baroclinic instability as demonstrated by *Gascard* [1978]; *Legg*
565 *and Marshall* [1993]; *Visbeck et al.* [1996]. During the restratification phase, very high
566 currents, mainly barotropic, order of 30–40 cm s⁻¹ can be observed at LION [*Houpert*
567 *et al.*, 2016]. This is consistent with the expected results of baroclinic instability with
568 a transfer of Available Potential Energy (APE, here considered as proportional to the
569 integral of potential density profiles) into Kinetic Energy (KE) and a barotropisation

¹¹Sorbonne Universités (UPMC Univ.

570 of the currents. The kinetic energy (KE) could be estimated from the depth-average
571 currents (average over 0–1000 m only) and the kinetic energy due to the fluctuations of
572 the currents, the Eddy Kinetic Energy (EKE), by considering those depth-average currents
573 minus a large scale depth-average current, low-pass filtered with a scale of 100 km along
574 the glider trajectories (Figure 5).

575 Noteworthy, the KE and EKE start to increase late January – early February when
576 the mixing reaches depths of about 1000 m (see Figure 4g). At this stage, the conversion
577 of potential into kinetic energy starts and this will increase until the system reaches a
578 maximum in potential energy. This clearly illustrates the violent mixing phase and the
579 spreading overlap. The maximum in potential energy is reached by early March. At
580 this stage, the heat fluxes at the surface are not able to extract sufficient buoyancy to
581 overcome lateral fluxes due to eddies. The maximum in EKE is reached about 2 weeks
582 later and this gives evidence to a response time scale for the development of instabilities
583 resulting in the break-up of the *Mixed Patch*. About half of the increase in KE is due
584 to eddies while the other half due to larger scale currents (the Northern Current and the
585 recirculation associated to the North Balearic Front south of the convection area). Deep
586 convection is thus associated with an increase in intensity of these large-scale circulation
587 features. This can be due to a large-scale response to the intensification of the lateral
588 gradients of density as the water column gets denser and denser through deep convection
589 processes in the *Mixed Patch*.

590 The non-filtered data in APE show large variations with a first peak mid-February
591 when deep convection first reached the bottom followed by scattered high and low values.

Pierre et Marie Curie, Paris 06), UMR

592 One can observe the same pattern again mid-March during and after the second deep
593 convection event. This illustrates the homogenization of the area during the deep mixing
594 events, while the area is characterized by both mixed profiles (high APE) and stratified
595 ones (lower APE). High values of non-filtered KE and EKE can be observed at the same
596 times but also later on, until the APE, KE and EKE reach low values again.

6.3. Spatio-temporal coverage and budgets estimates

597 Figure 6 shows analyses of MLD, averaged salinity over the surface layer (0–100 m),
598 averaged potential temperature over the intermediate layer (400–600 m), and average chl-
599 a profiles over the 0–300 m. Data are considered on the 10 km×10 km grid over periods
600 of 1 month with respect to the related first guess. Extrapolated values being estimated
601 to have an error of more than 95% (in terms of variance) based on the 75 km analysis are
602 shaded. It shows that the amount of collected information provides a convenient spatio-
603 temporal coverage and allows to describe the deep convection process on a continuous
604 basis at various scales throughout the year.

605 Figures 6a, b and 6c show there is a maximum salinity expression in the surface layers
606 and a minimum potential temperature expression at intermediate depths on the analyses
607 of 14 February concomitant with deep mixed layers (> 1000m). Winter mixing actually
608 transforms into deep convection at that time, once the winter mixing has eroded the LIW
609 layer. Then, the signal fades away, more quickly in the surface layers. Figure 6d presents
610 analyses of chl-a estimates averaged over 0-300m and it is consistent with Figure 4h and
611 4i. The development of the phytoplankton starts in the deep convection area as early as

7093, Laboratoire d’Océanographie de

612 September when the MLD starts to deepen. Later on, in February, phytoplankton seems
613 to develop around the *Mixed Patch* before the bloom in April. In April, chl-a estimates
614 present high values at the scale of the basin, from the Gulf of Lions to the Ligurian Sea,
615 and even higher values in the deep convection area. Then, phytoplankton disappears
616 rapidly with very low values everywhere in June.

617 The very large number of *in situ* observations harvested between January and May
618 allows to solve in a quasi-synoptic way the typical scales of deep convection, and the same
619 methodology was applied at a higher frequency. Figures 7 and 8 show high frequency
620 (10 days) analyses of the MLD and potential density at 1000 m depth respectively with
621 the related first guess being the previously described (monthly) analyses.

622 MLDs greater than 1000m depth can be observed starting in mid-January in the western
623 part of the Gulf of Lion and the surface of the *Mixed Patch* increases until the beginning
624 of March reaching a maximum extent of $28 \pm 3 \cdot 10^9 m^2$ late February. It then quickly
625 restratifies. The analyzed fields are sometimes patchy at the small scale but the general
626 evolution emerges well with a break-up starting late March. The deep mixing occurs at
627 the end of January with the formation of dense waters ($> 29.11 \text{ kg m}^{-3}$). The density of
628 the newly-formed waters increases after it has reached the bottom early February. The
629 newly formed deep waters are characterized at that time by a density anomaly of about
630 0.01 kg m^{-3} and this remains identifiable in the months that follow - in particular in April,
631 with a slow and general movement towards south and west. The amplitude of the density
632 anomaly decreases throughout the restratification processes until May, with a progressive
633 flattening of the isopycnals at the basin scale. These analyzed fields are consistent with

Villefranche (LOV), Observatoire

634 the time series of Figure 4 and describe the evolution of the area, with a lower time
635 resolution but a description of the spatial patterns associated with deep convection.

636 The 4D analysis in space and time of the density field in particular, allows us to analyze
637 the transformations of the water masses that take place within the deep convection area.
638 Figure 9a shows the evolution of the volume of water denser than certain selected potential
639 density thresholds, between mid-January and May. These estimates have been made over
640 a relatively large area but restricted to the box as displayed on figure 8, for a good coverage.
641 The total volume of water presenting potential densities $> 28.00 \text{ kg/m}^3$ (σ_0) in the area
642 under consideration is relatively constant over time, with a volume of $1.6 \cdot 10^5 \text{ km}^3$, the
643 volume under consideration being in fact composed quasi-totally by waters denser than $>$
644 28.00 kg/m^3 . The time series associated to denser waters volumes present increases, the
645 denser the later, as a result of transfers between the different isopycnal layers.

646 The relatively light waters presenting potential densities $< 29.11 \text{ kg/m}^3$ are progressively
647 transformed into denser and denser waters during the violent mixing events starting mid-
648 January for waters presenting potential densities $> 29.11 \text{ kg/m}^3$ and $< 29.115 \text{ kg/m}^3$, and
649 later on with the apparition of new waters presenting potential densities $> 29.115 \text{ kg/m}^3$
650 and $< 29.12 \text{ kg/m}^3$ early in February, and even denser new waters ($> 29.12 \text{ kg/m}^3$) mid-
651 February. During restratification periods, the opposite effect is observed: the volumes of
652 dense waters decreases, while they spread out of the area of the Gulf of Lions, mix with
653 other waters (with transfers from density classes to others) and light waters reinvest it.

654 The increase in volume is generally rapid for the different classes of water $> 29.11 \text{ kg/m}^3$
655 and followed by a general decrease. The fact that all these time series decay at about the

Océanologique de Villefranche/mer, France.

656 same rate denotes a general input of lighter waters that can be better observed on Figure
657 9b as the volume (averaged over a year and expressed in Sv in order to be compared with
658 other numbers that can be found in the literature) increases starting end of February for
659 waters presenting densities $<29.11 \text{ kg/m}^3$. After a transformation in denser waters, the
660 volume of this class of density increases from a minimum of -2.0 Sv (volume averaged over
661 a year) compared to the situation on 5th January 2013 at a rate opposite and equivalent
662 in magnitude to the general decrease of the volume of the denser water masses. At that
663 time the volume of waters $>29.11 \text{ kg/m}^3$ is consistently about $+2.0 \text{ Sv}$ (volume averaged
664 over a year). This illustrates that the process of deep water formation by deep convection
665 can be considered as a mass transfer that can be quantified, from the surface isopycnal
666 layers losing buoyancy due to air-sea interactions to the deep isopycnal layers.

667 The production of the densest waters ($> 29.12 \text{ kg/m}^3$) is estimated at 0.5 Sv (Figure
668 9b, volume averaged over a year) and occurs when the mixing reaches the bottom. At
669 that time, the atmospheric forcing remains intense for a while allowing to form even
670 denser deep waters [Houpert *et al.*, 2016]. This layer presents a volume that increases
671 until mid-March and decreases later on, as they spread and mix with lighter waters. The
672 volume of the waters presenting potential densities $> 29.115 \text{ kg/m}^3$ and $< 29.12 \text{ kg/m}^3$
673 increases up to a maximum of 1.5 Sv (averaged over a year) in mid-March (Figure 9b).
674 These deep waters form earlier with an increase in volume starting in early February and
675 a first relative maximum in volume in mid-February at the time of the first event of deep
676 convection. It then decreases until it increases again around mid-March at the time of

¹²Departamento de Oceanografía Física,

677 the second deep convection event, in a consistent way with Figure 4. The evolution of the
678 volume of the waters presenting potential densities $> 29.11 \text{ kg/m}^3$ and $< 29.115 \text{ kg/m}^3$
679 shows that they are the first to experience an increase of their volume during the winter. It
680 starts to increase in mid-January and reaches a maximum in mid-February. This increase
681 is followed by a slow but continuous decrease until May at about the same rate as for the
682 densest layers.

683 For 2013, we can conclude that deep-water formation has created water with potential
684 densities $> 29.11 \text{ kg/m}^3$ with a rate of formation which can be estimated to $2.0 \pm 0.2 \text{ Sv}$
685 (volume averaged over the year – see Figure 9c). In addition, this volume of deep water
686 can be decomposed into two main categories: (1) deep water having a density > 29.12
687 kg/m^3 formed around the end of February starting once the mixing layer has reached
688 the bottom (25% of volume formed); 2) deep water with a slightly lower density > 29.11
689 kg/m^3 formed starting at the beginning of February and composing most of the newly-
690 formed deep waters (75% of the volume). During the month of March, the second episode
691 of mixing, appears to only generate a second-order formation rate of 0.1 Sv compared to
692 the previous maximum observed in mid-February, the period of negative heat fluxes at
693 that time being possibly too short to have a real significant impact on the water column.

694 These approaches by density classes may suggest there are different types of newly-
695 formed deep waters but in reality this is more a continuum of newly-formed deep waters
696 presenting densities between 29.11 and 29.123 (the maximum observed density) as illus-
697 trated by Figure 9c which inventories the volume (averaged over a year) of the different
698 waters formed according to their density properties. Because it shows the dependency of

Centro de Investigacion Cientifica y de

699 the change of volume for waters having a greater density than, the production rate must
700 be determined by the maximum of the curve and is consistently about 2.0 Sv (volume
701 averaged over a year).

702 Finally, Figure 9d shows the volumes estimated using the MLD estimates which shows
703 that there is instantaneously about 3 times less waters in relatively shallow mixed layer
704 (deeper than 500 m) than in the very deep ones (deeper than 1000 m) with volume
705 estimates of maximum $710^{13}m^3$ and $510^{13}m^3$ respectively. The overall volume of newly-
706 formed deep waters that can be computed late February (when the volume is maximum)
707 from this method is about 1.4 Sv (averaged over a year) using $MLD > 1000m$ and about
708 2.0 Sv (averaged over a year) using $MLD > 500m$.

7. Discussion

709 The analyses presented above do not account for small-scale processes, except in the
710 'error' estimated on our $10km \times 10km$ grid. This is so not critical as far as budgets are
711 concerned but that somewhat hides a variety of processes at stake. After summarizing
712 important results about related numerical studies and discussing the robustness of our
713 deep water formation rate estimates, we will highlight in this section several peculiar
714 circulation features that could be observed. Our observations bring new knowledge on the
715 sub-mesoscale turbulence, the *plumes* in the *Mixed Patch* and the symmetric instability
716 at the edge of the *Mixed Patch* that are important to consider when studying with deep
717 convection and subsequent bloom because they are responsible for significant fluxes of
718 energy and (dissolved and particulate, organic and inorganic) matter – in particular while

Educacion Superior de Ensenada, Ensenada,

719 analyzing/interpreting the various biogeochemical measurements carried out during the
720 R/V cruises, and more especially during the DEWEX-1 and DEWEX-2 cruises which
721 collected numerous biogeochemical observations based on water samples.

7.1. Numerical model initialization/validation

722 The Summer data were used to correct initial conditions for modelling studies. As
723 pointed out by *Lger et al.* [2016], "*L'Hévéder et al.* [2013] and *Somot et al.* [2016], numer-
724 ical simulations are very sensitive to the initial conditions with regards to winter convec-
725 tion and numerical outputs, including operational products like MERCATOR PSY2V4R4
726 [*Estournel et al.*, 2016b], have generally serious difficulties to describe well the intermedi-
727 ate and deep layers, because stratification is influenced by initial conditions derived from
728 smoothed climatologies encompassing decades of observations. *Waldman et al.* and *Es-*
729 *tournel et al.* [2016b] showed it is possible to correct the initialization and forcing of their
730 model and to significantly improve the realism of the simulations using the DEWEX data
731 set both for initial conditions correction in Summer and later validation.

732 This data set was then used for validation purposes to assess the realism of numerical
733 simulations in particular in terms of timing and geography of the phenomena as well
734 as in terms of quantitative estimates of the deep water formation rate [*Waldman et al.*,
735 2016, 2017] and in terms of meso- and submeso- scale processes [*Damien et al.*, 2017;
736 *Waldman et al.*] by performing similar diagnostics in the observations and the simulations,
737 and sensitivity studies. They were thus able to reach a better understanding of deep
738 convection processes from autumn to winter together with quantitative estimates. They

Baja California, Mexico

739 were able in particular to estimate that lateral advection through the *Mixed Patch* could
740 represent 58% of the destratifying effect of surface fluxes when integrated over the winter.
741 This implies restratification must be considered as a major process during, and not only
742 after the end of, the violent mixing but not as important as in the theory of *Visbeck et al.*
743 [1996] in which lateral fluxes entirely balance the buoyancy loss through the sea surface,
744 certainly because deep convection reached the bottom this year which cast a limit to the
745 equilibrium depth solved in this study. The winter 2012-2013 is probably the third in
746 buoyancy loss intensity after 2005 and 2012 during the period 1980-2013 [*Somot et al.*,
747 2016] with more than 20 "stormy days" over the December-March period.

748 Another major outcome of this DEWEX experiment concerns the air-sea interactions.
749 It must be noted it was impossible to measure directly the air-sea turbulent fluxes and
750 that estimates of the total buoyancy losses are dependent on their parameterization. It
751 has not been particularly developed for strong winds as one can observe in this region in
752 winter and this can introduce some uncertainty on the role of the atmosphere. Thanks
753 to this data set, *Caniaux et al.* [2017] managed to propose an inverse method to estimate
754 during one year heat and water fluxes for the whole northwestern Mediterranean basin and
755 at a fine scale resolution (i.e. hourly fluxes and $0.04^\circ \times 0.04^\circ$ longitude, latitude) allowing
756 to close the heat and freshwater budgets. The comparison of these adjusted fluxes with
757 fluxes estimated at the LION buoy from in-situ meteo-oceanic measurements shows a
758 good correlation ($r^2 = 0.96$) and provides a validation of the parameterization used for

¹³CNRS-Université de Perpignan, Centre

759 the estimates of the turbulent air-sea fluxes from the LION buoy (see Caniaux et al.'s
760 Figure 9).

7.2. nWMDW formation rate estimates

de Formation et de Recherche sur les
Environnements Méditerranéens (CEFREM),
Perpignan, France.

¹⁴CNRS-Université de Toulouse,
Laboratoire d'Aérodynamique (LA), Observatoire
Midi-Pyrénées, Toulouse, France.

¹⁵Aix-Marseille Université, Université de
Toulon, CNRS, IRD, MIO UM 110, 13288,
Marseille, France

¹⁶MétéoFrance/CNRS, CNRM, UMR
3589, Toulouse, France.

¹⁷Ifremer-CNRS-IRD-UBO, LOPS,
IUEM, Plouzané.

¹⁸Sorbonne Universités (UPMC Univ.
Pierre et Marie Curie, Paris 06), UMR
7093, Laboratoire d'Océanographie
Microbienne (LOMIC), Observatoire
Océanologique de Banyuls/mer, France.

761 One shortcoming is that the frontier closing the domain used for estimating the deep
762 water formation rate (see Figure 8) is relatively close to the *Mixed Patch* on its south-
763 western part. This could lead to underestimations of the volume formed. However, the
764 dense water volume formed outside the domain is likely second order compared to our
765 estimates. MLD barely $> 750\text{m}$ (Figure 8) while potential densities $< 29.10 \text{ kg m}^{-3}$ (Fig-
766 ure 8) are observed along this frontier and the chosen domain likely captures the entire
767 deep convection process. In order to assess their robustness, our estimates of 2.0 Sv for
768 the production of newly-formed deep waters can be compared with estimates that can be
769 made from different methodologies.

770 As already pointed out in section 6.3 the volume of water formed could be estimated
771 assessing the maximum volume of the mixed layer greater than a given value, enough to
772 have mixed the LIW layer lying above the deep waters but this induces some uncertainties
773 related to the arbitrary choice of the threshold (see 9d : 1.4 Sv for MLD $> 1000\text{m}$, 2.0Sv
774 for MLD $> 500\text{m}$). Another but similar method is to use satellite ocean color images
775 as in *Houpert et al.* [2016] and *Herrmann et al.* [2017], when the cloud coverage allows
776 exploiting some images of the deep convection area. The strategy is to identify the 'blue
777 hole' associated to *Mixed Patch* within restratifying waters around. In 2013, using Figure
778 2e and estimating the 'Blue Hole' surface with a threshold value of Chl-a $< 0.15 \text{ mg m}^{-3}$
779 yields to $23\,583 \text{ km}^2$. Considering an average depth of 2200 m in the convection zone,
780 the winter 2013 would thus present a production rate of 1.6 Sv (on average over the
781 year). Again, it must be noted this method is very sensitive to the threshold (here in
782 chl-a concentration): considering a slightly different threshold in Chl-a concentration of
783 $< 0.25 \text{ mg m}^{-3}$ would yield in fact to a doubling of the volume of the newly-formed deep

784 waters. There is so a strong need to accurately define the threshold in chl-a concentration
785 used for such estimates. The choice of $< 0.15 \text{ mg m}^{-3}$ can actually be justified by
786 data from gliders crossing the edge of the *Mixed Patch* at about the date of the satellite
787 image [Houpert et al., 2016]. They show that deep mixed layers are associated with chl-a
788 concentrations lower than this value this year but the right threshold is not necessarily the
789 same every year and it is important to note there is a need to carry out such measurements
790 in the long term if one wants to address interannual variability using this method.

791 Our estimates from in-situ data based on density classes are similar in magnitude to
792 those estimates but still larger by about 0.0-0.6 Sv (on average over a year). On the
793 other hand, such estimates are likely to underestimate the deep water formation rate first
794 because they do not account for lateral fluxes. Moreover, the process of deep water renewal
795 is a process that is not instantaneous and estimates made on the basis of an instantaneous
796 image or snapshot inevitably underestimate the volume of newly formed deep waters. The
797 dates of analyses of MLD (every 10 days) and the available satellite images (with small
798 cloud cover) do not necessarily correspond to the date of the maximum extent of *Mixed*
799 *Patch* (Blue Hole) and restratification processes are able to quickly recap mixed layers
800 possibly hiding volumes of newly-formed deep waters under the surface. Still, it is quite
801 appealing that the estimates based on a single analysis or a single ocean color image are
802 in such a good agreement with our present ones based on density classes.

803 Other estimates were performed by Waldman et al. [2016] using analyses of ship CTD
804 data only and the deep water formation rate was estimated to be 2.3 ± 0.5 Sv. Ship data are
805 the only data except for the mooring data that characterize the deep layers and the cruise
806 plans were designed to estimate such volumes with large-scale surveys. Using an OSSE

807 approach based on the simulation presented in *Estournel et al.* [2016b], *Waldman et al.*
808 [2016] assessed the capacity of the CTD array to capture seasonal dense water variations,
809 in terms of spatial distribution and the results indicate a low uncertainty related to space
810 and time undersampling of the observing network because the cruises carried out at large
811 scale provide integrated information. Our present estimates of newly-formed dense water
812 volumes certainly rely on the same deep data and the estimates are consistently similar.
813 The methodologies proposed for estimating the deep convection rate are complementary.
814 In particular, *Waldman et al.* have shown from a modeling study that the *Mixed Patch*
815 volume computed as the volume of $MLD > 1000\text{m}$ (or from a cold signature ($< 13^\circ\text{C}$) of
816 intermediate waters (400-600m)) reached a lower value by $1.5 \times 10^4 \text{km}^3$ (0.4 Sv averaged
817 over a year) than the dense water formation rate computed with the volume of waters
818 denser than 29.11kg/m^3 in their run. Both estimates have different physical origins,
819 the former resulting exclusively from the intense vertical mixing during the deep water
820 formation events and the latter also resulting from lateral advection and mixing with
821 surrounding waters.

822 Noteworthy, we present here a methodology that allows such estimates to be augmented
823 with the data from the numerous autonomous platforms (gliders, profiling floats, moor-
824 ings, drifter) that could continuously observe dense waters (Figure 9), sometimes only
825 above 1000 m (gliders and floats) or 2000 m (floats) depths but this additional informa-
826 tion is very significant, helping to describe the timing of the production at higher frequency
827 as well as transfers between different classes of density. Compared to few satellite images in
828 months, or 1-6 times a year thanks to MOOSE-GE-like cruises, the 10-days analyses based
829 on in-situ data represent a breakthrough for describing the deep convection phenomenon.

7.3. SCVs

830 As described more thoroughly in [Bosse, 2015], glider data revealed for the first time very
831 warm (+0.4°C) and saline (+0.1) submesoscale and lenticular anticyclones at intermediate
832 depth characterized by a small radius (5km) and high Rossby (0.3) and Burger (0.7)
833 numbers. Their cores are composed of marked LIW. Figure 10a shows two of them on
834 the same glider section and this illustrates how numerous they can be. Roughly ten are
835 formed each year contributing significantly to the spreading of the LIW toward the sub-
836 basin interior. They have a lifetime order a year and can be quite numerous in the whole
837 basin. They would be mainly formed by the combined action of turbulent mixing and flow
838 detachment of the northward flow of LIW at the northwestern tip of Sardinia. Upwelling
839 conditions along the western coast of Sardinia associated with a geostrophic southward
840 surface flow could also play a key role in their formation process. These "Suddies" contain
841 LIW from the formation region that is protected from mixing with the surroundings by
842 dynamical barriers due to the high non-linearity of the SCV flow Bosse *et al.* [2017]. They
843 have thus a potential impact on winter mixing because they correspond to salt/heat inputs
844 at intermediate depths and are associated with dynamical preconditioning of mixing (local
845 doming of isopycnals). About 2-3 (or more?) of these eddies could be present in the deep
846 convection area (as suggested by Figure 10a) and expose such LIW (and all associated
847 dissolved or particle organic and inorganic matters) to winter mixing. The stratification
848 index of such eddies shows they are preconditioning agents and deep convection will
849 preferentially develop in these flows. In terms of ecosystem functioning this could be a
850 direct route from the SCV formation locations (mainly the northwestern tip of Sardinia)
851 to the deep convection area and contact with the atmosphere.

852 In addition, *Bosse et al.* [2016] identified other SCVs, remnants of wintertime deep verti-
853 cal mixing events. Figure 10b shows a transect across the boundary circulation (Northern
854 Current and the south recirculation associated with the North Balearic Front) and the
855 *Mixed Patch* with *Transition Zones* in-between, where SCVs can be observed, just expelled
856 from the homogeneous *Mixed Patch*. Figure 10c also shows two of them (one cyclonic and
857 one anticyclonic) on the same glider section, which again illustrates how numerous these
858 eddies can be in Spring. This documents the spreading phase of deep convection with dif-
859 ferent eddies presenting different characteristics in temperature and salinity. These SCVs
860 are though all characterized by a small radius ($\sim 5\text{--}8$ km), mostly strong depth-intensified
861 orbital velocities ($\sim 10\text{--}20$ cm s $^{-1}$) with sometimes a surface signature, high Rossby (~ 0.5)
862 and Burger numbers $O(0.5\text{--}1)$. Anticyclones are found to transport newly-formed waters
863 resulting from vertical mixing characterized by intermediate ($\sim 300\text{m}$) to deep (~ 2000 m)
864 mixing. Cyclones are characterized by a thick layer ($\sim 500\text{--}2000$ m) of weakly stratified
865 newly formed deep waters likely extending from the bottom of the ocean (~ 2500 m).
866 Cyclones extending from the surface to the bottom have also been observed. All these
867 SCVs result from intrusions of mixed fluid parcels into a more stratified environment and
868 followed by cyclogeostrophic adjustment. Noteworthy, the formation of cyclonic eddies is
869 favored in 2013 once the convection reached the bottom because this implies a limit in
870 the adjustment phase and prevents the formation of anticyclones composed of nWMDW.

871 Both anticyclonic and cyclonic SCVs have a prominent role in the spreading of the
872 newly-formed deep waters away from the winter mixing areas. Since they can survive until
873 the following winter, they can greatly populate the basin and also have a great impact on
874 the mixed layer deepening through a local preconditioning effect. These SCVs consist in

875 another type of preconditioning agents like the above mentioned Suddies. Moreover, they
876 can be formed throughout the deep convection mixing phase and modulate at this scale
877 the vertical mixing occurring in *Plumes* during the violent mixing phase as well.

878 As reported by *Bosse et al.* [2017] they have a significant impact on the distributions
879 of biogeochemical properties with clear signatures on the dissolved matter (nutrient and
880 dissolved inorganic carbon in particular), compared to the surroundings. SCVs cores con-
881 tain concentrations that are very contrasted with the general deep concentrations, being
882 composed of waters resulting from a mixing of surface waters with deeper waters. This in-
883 troduces a granularity at the SCV scale in the distributions of the biogeochemical variables
884 in the basin since SCVs export these waters throughout the basin. Finally, these eddies
885 have a peculiar impact on suspended particles distribution. As reported by [*Durrieu de*
886 *Madron et al.*, 2017], there is evidence of bottom thick nepheloid layer formation coin-
887 cident with deep sediment resuspension induced by bottom-reaching convection events.
888 This bottom nepheloid layer, which presents a maximum thickness of around 2000 m in
889 the center of the convection region, can persist within cyclonic nWMDW SCVs that are
890 formed during the convection period and can last several months while traveling through
891 the basin, still being associated with thick nepheloid layers far from the deep convection
892 area. They are thus key mechanisms that control the concentration and characteristics
893 of the suspended particulate matter in the basin, and in turn, affect the bathypelagic
894 biological activity.

895 *Waldman et al.* [2017] and *Waldman et al.* and have studied the impact of oceanic
896 intrinsic variability on deep water formation with eddy resolving and permitting simula-
897 tions. By comparing ensemble results they conclude mesoscale could have a significant

998 impact on deep water formation. Resolving mesoscale significantly improves the realism in
999 particular of the restratification/spreading phase and the *Mixed Patch* shape and extent.
900 These are first estimates of the impact of such eddies even if the eddy-resolving simulation
901 could not really account for SCVs. With a horizontal resolution of $1/36^\circ$ (about 2 km), the
902 simulation can actually not produce explicitly circulation features characterized by a ra-
903 dius order of 5km but represent them thanks to subgrid parameterizations constrained by
904 larger scale, but realist, variability and that allows a first assessment. The large increase
905 of ocean intrinsic variability in eddy-resolving, compared to eddy-permitting, simulations
906 and of its impact on deep water suggests that SCVs could contribute largely to the chaotic
907 ocean variability. Noteworthy, *Damien et al.* [2017] presented simulations which are the
908 first ones to our knowledge that are able to simulate SCVs with similar dynamical char-
909 acteristics and lifetimes in fully realistic conditions. A 1 km horizontal resolution and a
910 great control of tracers and momentum horizontal diffusion seem to be decisive features to
911 accurately resolve SCVs. This numerical study reveals itself particularly useful for refining
912 the estimation of their integral effect and tracking them over their entire lifetimes. Further
913 studies assessing the role played by SCVs in deep water formation (preconditioning, vio-
914 lent mixing and spreading at basin-scale and interannual time-scale) and furthermore, in
915 the different biogeochemical cycles that are identified in present biogeochemical numerical
916 models forced by physical ones are now possible.

7.4. Plumes

917 *Margirier et al.* present a methodology based on a glider quasi-static flight model that
918 was applied to infer the oceanic vertical velocity signal from the glider navigation data.
919 Figure 11 shows an example showing the vertical trajectory of the glider being modified

920 by vertical currents, the so-called *plumes*, and their estimates. Noteworthy, on the first
921 apogee, one can see the glider was undergoing strong downward currents. It has nearly
922 ended up with the loss of the glider (pressure rated to only 1000 m) but the glider forward
923 motion capacity allowed it to cross the vertical stream in about 10 min, and to reach a
924 safer area, characterized by upward velocities. This illustrates the vertical currents are
925 order of, and fortunately generally lower than, the vertical speed relative to water that
926 glider can have, typically about $10 - 20 \text{ cm.s}^{-1}$.

927 The data collected during winter 2012–2013 allows a first in situ statistical and 3D
928 characterization of the so-called *plumes* that are important mixing agents. During the
929 active phase of mixing, significant oceanic vertical velocities (upward and downward, up
930 to 18 cm.s^{-1} jostled the gliders. The gliders crossed many downward *plumes* with a mean
931 radius of about 350 m and distant from each other by about 2 km on average. The
932 upward part of the *plumes* is less coherent but apparently organized in crowns around the
933 downward plumes. Much higher downward velocities were observed, with a magnitude
934 about three times as large as that of the upward ones on average (-6.3 cm.s^{-1} versus
935 $+2.3 \text{ cm.s}^{-1}$).

936 On average, the *plumes* cover 27% of the convection area and the upward motion as-
937 sociated with them covers 71%. The total of 98% provides confidence in coverage of the
938 area. These are useful estimates to parameterize deep convection in ocean general circu-
939 lation numerical models. A specific parameterization of convection has been introduced
940 in atmospheric numerical models long ago but not yet in oceanic ones. Until now, oceanic
941 numerical models that would need such a parameterization to represent mixing do use
942 artificially increased diffusion instead. These results can now be used for the develop-

943 ment and the testing (with all the data collected during our study period) of a convection
944 parameterization in oceanic numerical models, following similar developments in meteo-
945 rology for convection in the atmosphere that use the convective fraction of a grid cell as
946 a key parameter, and further progress in modeling the deep convection processes can be
947 soon expected.

948 The structure in temperature and salinity as well as biogeochemical properties (dissolved
949 oxygen, fluorescence, turbidity) associated to this *plumes* is as follows: the downward
950 waters are saltier (+0.001), colder (-0.005°C) and thus denser (0.0015 kg m^{-3}) than the
951 surrounding upward ones. The downward waters are also slightly richer in oxygen and
952 less fluorescent. This confirms the downward *plumes* participate to the ventilation of
953 the waters and a dilution effect on Chl-a estimates (already mentioned previously when
954 commenting Figure 4) while in the upward parts of the plumes, phytoplankton would
955 benefit from nutrients being brought to the surface layers. On the other hand, there is no
956 mean correlation on the turbidity signals despite individual signals in *plumes* but going
957 both directions and this compensates on the average. The role of plumes as mixing agents
958 on the suspended material distribution likely results from various factors. There could be
959 some passive advection of turbidity signals from the surface (bloom) but also sometimes
960 from the nepheloid layer when the mixing reaches it. In the deep convection region,
961 intense horizontal currents favor resuspension over thick layers (100s m), with often a
962 higher expression in turbidity in that layer than at the surface. In addition, suspended
963 material have proper vertical downward speed and that increases the complexity of the
964 suspended material fluxes in the presence of *plumes* tickling this nepheloid layer and
965 lateral advection, through SCVs in particular.

7.5. Symmetric instability

966 Figure 12 illustrates the symmetric instability phenomenon presenting interleaving pat-
967 terns at the edge of the deep convection area over 0-500 m along the vertical and 20km
968 along the glider track. Figure 10 also shows similar patterns north and south of the deep
969 convection area, with alternating cold and warm waters circulating respectively down-
970 ward/outward and upward/inward of the deep convection area. Figure 12 provides a
971 zoom and documents this circulation feature that has a signature on all measured vari-
972 ables with tongues of alternating high and low values in temperature and salinity but also
973 in dissolved oxygen, chl-a concentration estimates and turbidity. Noteworthy are the high
974 chl-a estimates where the interleaving connects to the surface Figure 12d.

975 Almost all glider sections across the edge of the *Mixed Patch* exhibited similar inter-
976 leaving patterns during the mixing period as shown in Figure 12. In the ocean, the lateral
977 shears, fronts, and preexisting eddies make the horizontal gradients of density in mixed
978 layers, thus the thermal wind build up. If the slope of the buoyancy surface is steeper
979 than the absolute momentum surface, the slantwise convection will occur to release sym-
980 metric instability. That can propagate below the mixed layer and produce circulation
981 features responsible for the observed interleaving patterns. As indicated by [Marshall and
982 Schott, 1999] the slantwise convection induced by symmetric instability could maintain a
983 vertical stratification in the region that is being actively mixed. Using in particular the
984 data collected during our study period, Bosse [2015] showed that symmetric instability
985 can develop particularly at the edge of the *Mixed Patch*, mainly where wind and currents
986 flow along the same direction, and that it is possibly a major mixing process, like *plumes*,
987 that needs to be taken into account to try to fully comprehend the deep convection phe-

988 nomenon. The data collected by the gliders did allow to estimate the fluid Potential
989 Vorticity (PV) and often showed patches of negative PV at the edge of the *Mixed Patch*,
990 presenting a horizontal scale of a few km and a vertical one of hundreds of meters. It
991 is noteworthy the negative PV estimates are underestimated in absolute value. In fact,
992 the gliders do not always sample the ocean exactly along the density gradients, which are
993 thus underestimated, and if negative values could be observed, larger areas are certainly
994 characterized by (and even more) negative PV values in reality. These negative patches
995 indicate the edge of the *Mixed Patch* is a region where symmetric instability can develop
996 even more broadly than in these local patches.

997 The glider data did allow estimates of the vertical velocities associated with plumes but
998 not the part associated with symmetric instability. Estimating such vertical velocities
999 is actually a major challenge for oceanography today. This type of signal is impossible
1000 to measure directly by in situ observations because of the weak signals of 1-10 mm/s
1001 that are supposed to be associated with such circulations. In addition, these vertical
1002 velocities are concentrated in small-scale and rapidly evolving flows that are non-linear
1003 and ageostrophic [Mahadevan, 2006; Thomas et al., 2008]. They are weak, but relatively
1004 steady and so important in terms of fluxes, compared to oscillating movements due to
1005 internal waves that likely mask them with vertical velocities of the order of 1 cm/s and
1006 this is even more the case with higher velocities observed in *plumes* during the violent
1007 mixing phase.

1008 Analyzing numerical outputs in details can provide a clearer perception of this process.
1009 Using the NEMO model, Giordani et al. [2017] shows the edge of the *Mixed Patch* is
1010 a zone where negative PV can be observed and symmetric instability can develop as in

1011 the observations. In the high resolution (1km) SYMPHONIE model as well (see *Damien*
1012 *et al.* [2017] for a model description), there is a dominant and persistent negative PV
1013 frontal region of the Northern Current, where symmetrical instability can develop [*Bosse*,
1014 2015] and *Estournel et al.* [2016b] showed that destratification of the surface layer in
1015 autumn occurs through an interaction of surface and Ekman buoyancy fluxes associated
1016 with displacements of the North Balearic front bounding the convection zone to the south.
1017 The Ekman buoyancy fluxes appear to be important also in autumn, deepening the mixed
1018 layer in the southwestern part of the cyclonic gyre, increasing the size of the preconditioned
1019 area, and possibly feeding such symmetric instability processes throughout the year when
1020 the wind is blowing down front.

1021 The phenomenon can be described as follows. When the wind blows in the down front
1022 direction, the Ekman transport carries denser waters towards less dense waters. This
1023 induces not only a buoyancy flux but also the development of the symmetric instability
1024 phenomena with an associated steepening of isopycnals and increase of horizontal currents.
1025 This generates a potentially large turbulent mixing compared to the effect of surface
1026 buoyancy losses. This mechanical effect is important as indicated by *Giordani et al.* [2017]
1027 who estimated it is order of 4000 W m^{-2} , about 4 times the maximum buoyancy losses
1028 at surface. The PV shows negative values when the front is particularly steep (steeper
1029 than momentum surfaces) and this indicates where/when the flow is unstable. The region
1030 of negative PV is characterized by a marked ageostrophy which tends to accentuate the
1031 destabilization of the fluid and to induce vertical motions trying to bring the fluid back
1032 to a geostrophic balance. At the interface between negative and positive PV, vertical
1033 velocities of about 100 m day^{-1} can develop tending to bring fluid particles of positive

1034 vorticity towards the surface and negative vorticity to greater depth. Thereafter, the
1035 front would evolve rapidly towards a more stable situation with less inclined isopycnals
1036 and a wider frontal area. In both observations and numerical simulation, the effect of this
1037 instability can be observed over great depths, much deeper than the mixed layer above.

1038 The negative PV regions tend to fade away after about 24 hours in the model simula-
1039 tions. Consequently, the frequent physical and biogeochemical observations carried out
1040 by gliders that suggest strong vertical motions, because of the observed interleaving of the
1041 different physical and biogeochemical observed variables and negative PV estimates, may
1042 be only observations of remnants of vertical motions due to symmetric instability. Though
1043 they provide clear evidence of the prominence of this phenomenon, higher repeat rates
1044 for glider observations would be required to actually resolve it. Crossing the northern
1045 Current and the frontal area (about 30-50km width) takes about 1 or 2 days for a single
1046 glider and more gliders along the same repeat-sections would be required to increase the
1047 repeat rate if one wants to really capture this phenomenon.

1048 Overall, symmetric instability appears to be a major process in deep convection inducing
1049 water masses mixing during the three deep convection phases as suggested by the high
1050 number of occurrences of glider observations of this phenomenon throughout the year
1051 and the numerical simulations. Vertical motions can be indeed induced during any down
1052 front wind event. This could be active at high temporal frequency and participate to a
1053 significant part of the water formed by intermediate and deep convection during winter
1054 and more indirectly throughout the year by participating to the preconditioning of the
1055 area. This could also explain why the mixing seems to occur preferentially during the

1056 first stages in the western part of the Gulf of Lions (see Figure 7), where northerly winds
1057 blow down front, above a southward ocean general circulation.

8. Conclusions and outlook

1058 In this review we have attempted to draw together results of observations and numeri-
1059 cal experiments in the context of 2012-2013 DEWEX field campaigns, to summarize our
1060 current understanding of the underlying hydrodynamic processes at work before, during
1061 and after deep ocean convection events in the northwestern Mediterranean Sea and the
1062 interplay between the large scales, meso-scales, submeso-scales and convective scales. This
1063 interplay is complex since it involves scales, ranging from the scale of the general circula-
1064 tion, right down to the plumes at scales of < 1 km, through eddies about the deformation
1065 radius ($O(5\text{km})$ during winter period in the mixing area). As Marshall and Schott (1999)
1066 pointed out, a major challenge is to transform the obtained insights into parametric repre-
1067 sentations that address the complex 3-D nature of the processes at work. We have made
1068 a major step forward in that direction, about 15 years later, with a better description
1069 of the processes thanks to the autonomous platform technology, and can now consider
1070 not only some qualitative but also some quantitative aspects concerning deep convection.
1071 Deep convection is very difficult to observe due to its multi-scale variability and because
1072 it happens during severe weather events that generally prevents the use of ships. We
1073 have demonstrated that the massive –and artful– deployment of autonomous platforms
1074 in combination with more classical research cruises, can change the way we perceive the
1075 oceanic environment, allowing us to reach a much better spatio-temporal coverage. There
1076 is a paradigm change with the use of mobile platforms, such as gliders and profiling
1077 floats. Although, this concerns a limited number of physical and biogeochemical variables

1078 (the ones measured by miniaturized sensors that can equip such platforms: temperature,
1079 salinity, currents, oxygen concentration, chl-a concentration, turbidity estimates, etc.),
1080 this allows to better comprehend the deep convection and subsequent bloom phenomena
1081 at various scales.

1082 Deep convection and subsequent bloom have revealed ever greater complexity. Note-
1083 worthy are key elements that appear to be prominent for deep convection and subsequent
1084 bloom. The summer stratification is certainly key as it will be eroded continuously un-
1085 til the vertical mixing reaches great depths. Horizontal inhomogeneities in density in
1086 the mixed layer modulate its deepening, while fronts sharpen and (baroclinic) instability
1087 processes develop and produce a mesoscale turbulence. When the vertical mixing has
1088 eroded the LIW layer, it can reach quickly great depths (in about 1-2 weeks) and produce
1089 nWMDW resulting from mixing of the underlying WMDW with the water resulting from
1090 the mixing of AW and LIW above. Plumes develop with a downward plume radius of
1091 about 350m over a turbulent flow presenting a scale of about 5km embedded in the gen-
1092 eral circulation an ultimately forming the long-lived SCVs. The location of such intense
1093 vertical mixing is mainly due to preconditioning effects at various scales (gyre, mesoscale,
1094 submesoscale) as sketched in Figure 13, that is interesting to consider together with Fig-
1095 ures 6, 7 and 8 for the large scale aspects and Figures 10 and 12 for the smaller ones.
1096 Submesoscale turbulence and horizontal transfers shape a deep mixing area in the center
1097 of the basin gyre circulation that is surrounded by a *Transition Zone* where lateral ex-
1098 changes are prominently located between the Mixed Patch and the boundary circulation
1099 (Northern Current and its recirculation along the North Balearic Front). In about 1-2
1100 weeks, several storms induce several mixing events and restratification ones in-between

1101 that ultimately produce a water column that is mixed from the surface to the bottom.
1102 The SCV phenomenology appears to be key for understanding the deep convection pro-
1103 cess because of their role in preconditioning and lateral exchanges. In addition, symmetric
1104 instability develops along fronts under down front winds, which vertically and horizon-
1105 tally mixes the waters from each side of the fronts and make typical interleaving pattern
1106 emerge. The preconditioning and the spreading occur during the violent mixing phase.
1107 When the buoyancy loss stops, much of the flow and the spreading of water masses is
1108 eddy-dominated and highly variable while serious recapping processes concur due to both
1109 heat (and freshwater) gain and oceanic instabilities. Herein lies the reason why deep con-
1110 vection is such an interesting phenomenon from a theoretical point of view and why it is
1111 such a challenging and demanding process to observe and model.

1112 Our multi-platform approach allowed to have more synoptic observations and provided
1113 new results on deep convection. This can be considered as a major step forward com-
1114 pared to previous studies limited to very few in situ observations of the water column.
1115 Our observations allow performing first budgets and assessments with a continuity and
1116 accuracy that was never reached before in terms of potential temperature, salinity, MLD,
1117 APE, KE, EKE, formation rates but also estimates of chl-a based on in situ data. They
1118 also provide a new and nice description of several types of the SCVs, especially along
1119 the vertical, including new (or first time identified as such) circulation features like the
1120 long-lived cyclonic SCVs. They also allowed a first statistical description of plumes and
1121 provided a first in-situ indication of the importance of symmetric instability, all around
1122 the deep convection area, down front winds in meanders in the South and in a more
1123 pronounced way along the Northern Current where the topographic constraint orients

1124 more generally the flow along Mistral and Tramontane winds. Not only the processes
1125 are becoming clearer from a physical point of view but also their prominent impact and
1126 significance for biological processes.

1127 The budgets and diagnostics presented in this paper can be made in numerical models
1128 as well and we advocate that models should be able to produce the same results as
1129 presented here, to be considered as presenting a high realism in simulating the deep
1130 convection process (and subsequent bloom) and as able to provide relevant conclusions on
1131 particular processes and climate projections. The observations carried out in 2012-2013
1132 could be considered as a first benchmark and a lot of further progress in the (physical and
1133 biogeochemical) modelling of deep convection, and subsequent bloom phenomena can be
1134 expected by further comparing these observations and numerical simulations.

1135 Moreover, the data set collected from ships and autonomous platforms (gliders, profiling
1136 floats, moorings, surface drifters) offers an invaluable context for observations based on
1137 water samples from ship data. While ship surveys allowed delayed-mode quality control for
1138 data collected by autonomous platforms, they were augmented by a better spatio-temporal
1139 coverage for a few physical/bio-optical variables. Noteworthy, this could be extended to
1140 estimate budgets for other variables with conditional objective analyses methods and work
1141 is in progress to estimates budgets for biogeochemical variables that are more scarcely
1142 observed. Furthermore, with the addition of numerical modeling and data assimilation, a
1143 further insight of the deep convection and subsequent bloom phenomena can be reasonably
1144 expected. The DEWEX framework has already motivated many studies based on both
1145 observations and modeling and this will undoubtedly furthermore developed, in particular
1146 with respect to biogeochemical theory and modeling. Many studies have already used this

1147 wonderful data set and many others can be legitimately anticipated. There is still a lot
1148 to investigate and we dare anticipate this will go beyond this special issue.

1149 It was urgent and timely to carry out this experiment, in such a way a first spatio-
1150 temporal coverage (from and in situ observing point of view) providing adequate initial-
1151 ization information is available for 2012-2013, while embedded in the less intense but on
1152 the long term observational framework of MOOSE. While the fluxes (from atmospheric
1153 models) are more and more validated, the monitoring of some of the resultant changes in
1154 the system is now feasible with modern techniques, and this must be done from now in a
1155 more global and fit-for-purpose Mediterranean GOOS (Global Ocean Observing System)
1156 programme encompassing the whole Mediterranean Sea that can address critical societal
1157 issues at this scale. In the future, the knowledge will narrow and more frequent (spatio-
1158 temporal) data set will be possible and required to further investigate and monitor the
1159 processes. There must be concerted efforts in developing both the spatio-temporal cover-
1160 age of the in-situ observing systems (in combination with satellites) and the number of
1161 variables that can be observed in an autonomous way. The long-term observations will
1162 serve as a backbone for further understanding at the process level on an interannual basis
1163 while one can anticipate further and more intense process studies will be developed. As the
1164 miniaturization of sensors will increase, the number, the diversity of platforms and sensors
1165 on-board will likely unlock our knowledge on many processes/cycles, and transports of
1166 energy and various matter in the ocean.

1167 We presented an approach that was not only quite successful but especially scalable,
1168 and this motivates to develop the same multi-platform/multi-scale strategy for other ar-
1169 eas/processes. What has been learned about how to operate such a complex program is

1170 that preparation, coordination and funding are key aspects and it was only possible to
1171 achieve it building on several national and European infrastructures and several research
1172 programs. No call for proposals could be solely solicited to achieve such an experiment and
1173 we hope this will change in the future for the sake of simplicity and continuous knowledge
1174 improvements.

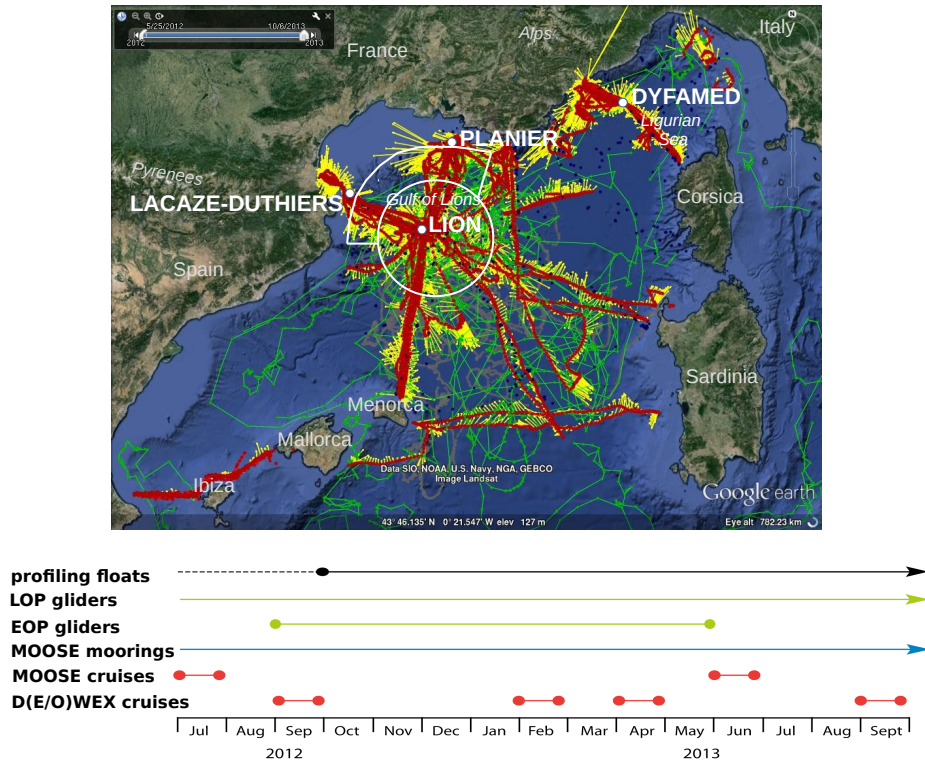


Figure 1. All observations carried out between 1st July 2012 and 1st October 2013. Gliders surface positions (red dots) and measured depth-average currents (yellow arrows). Profiling floats surface positions and trajectories (green). CTD casts from research cruises (blue). Surface drifters trajectories (grey). Positions of the LION, LACAZE-DUTHIERS, PLANIER, and DYFAMED moorings (white dots). The two selection areas "Boundary Current" and "Mixed Patch" used in Figure 4 are displayed in white.

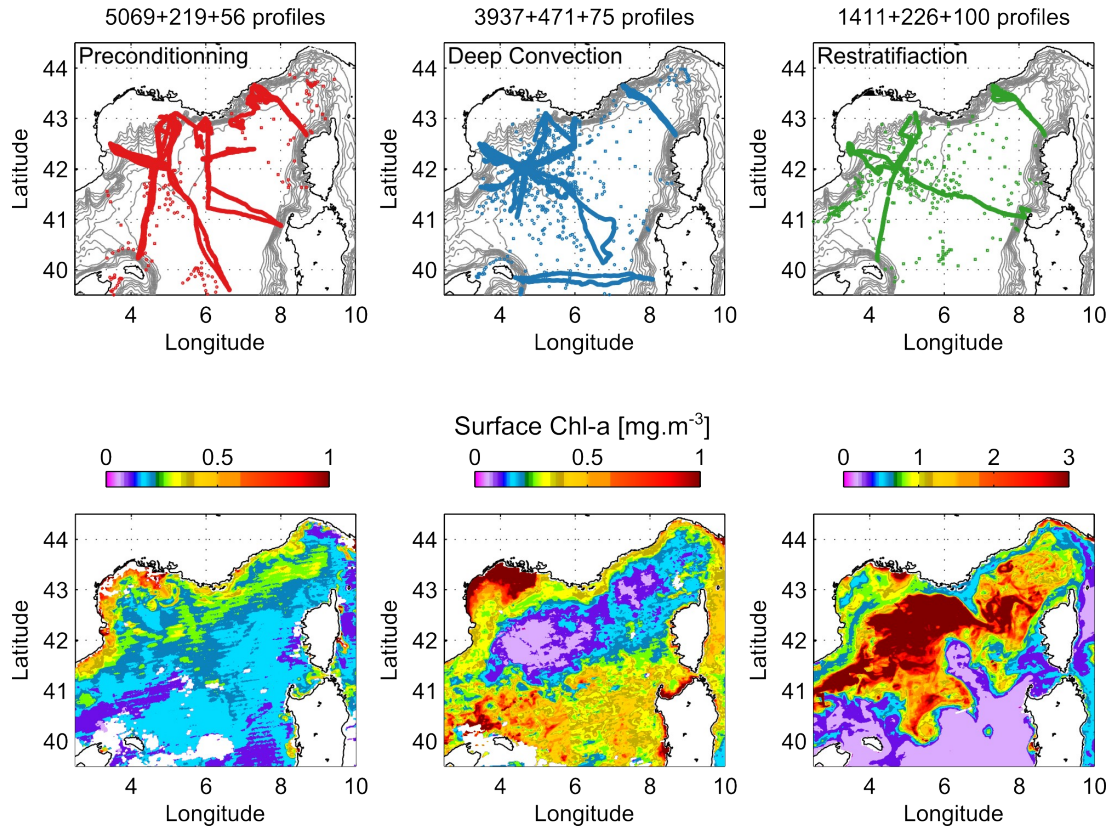


Figure 2. (top) Spatial coverage during the so-called "preconditioning" (Sep 1–Dec 15, 2012), "mixing" (Dec 15, 2012–Mar 31, 2013) and "restratification" (Apr 1–May 31, 2013) phases of deep convection. The number of profiles respectively collected by gliders, Argo profiling floats and R/V is indicated. (bottom) Surface chlorophyll-a concentration retrieved by satellite (L3 MODIS product) and averaged on November 1–2, 2012 (left), February 13–21, 2013 (middle), April 12–14, 2013 (right) that correspond to cloud-free periods during each phase.

Cruises names	Ships	Dates	Reference
MOOSE-GE 2012	R/V Le Suroît	July 2012	[<i>Testor et al.</i> , 2012]
DOWEX 2012	R/V Tethys II	September 2012	[<i>Mortier</i> , 2012]
HyMeX SOP1	R/V Urania, R/V Le Provence	September 2012 and October 2012	[<i>Ducrocq et al.</i> , 2014] [<i>Taupier-Letage</i> , 2013]
DEWEX-1	R/V Le Suroît	February 2013	[<i>Testor</i> , 2013]
HyMeX SOP2	R/V Tethys II, R/V Le Provence	January, February, March, and May 2013	[<i>Estournel et al.</i> , 2016a] [<i>Taupier-Letage and Bachelier</i> , 2013]
DEWEX-2	R/V Le Suroît	April 2013	[<i>Conan</i> , 2013]
MOOSE-GE 2013	R/V Tethys II	June 2013	[<i>Testor et al.</i> , 2013]
DOWEX 2013	R/V Tethys II	September 2013	[<i>Mortier and Taillandier</i> , 2013].

Table 1. List of cruises carried out in the framework of the DEWEX experiment.

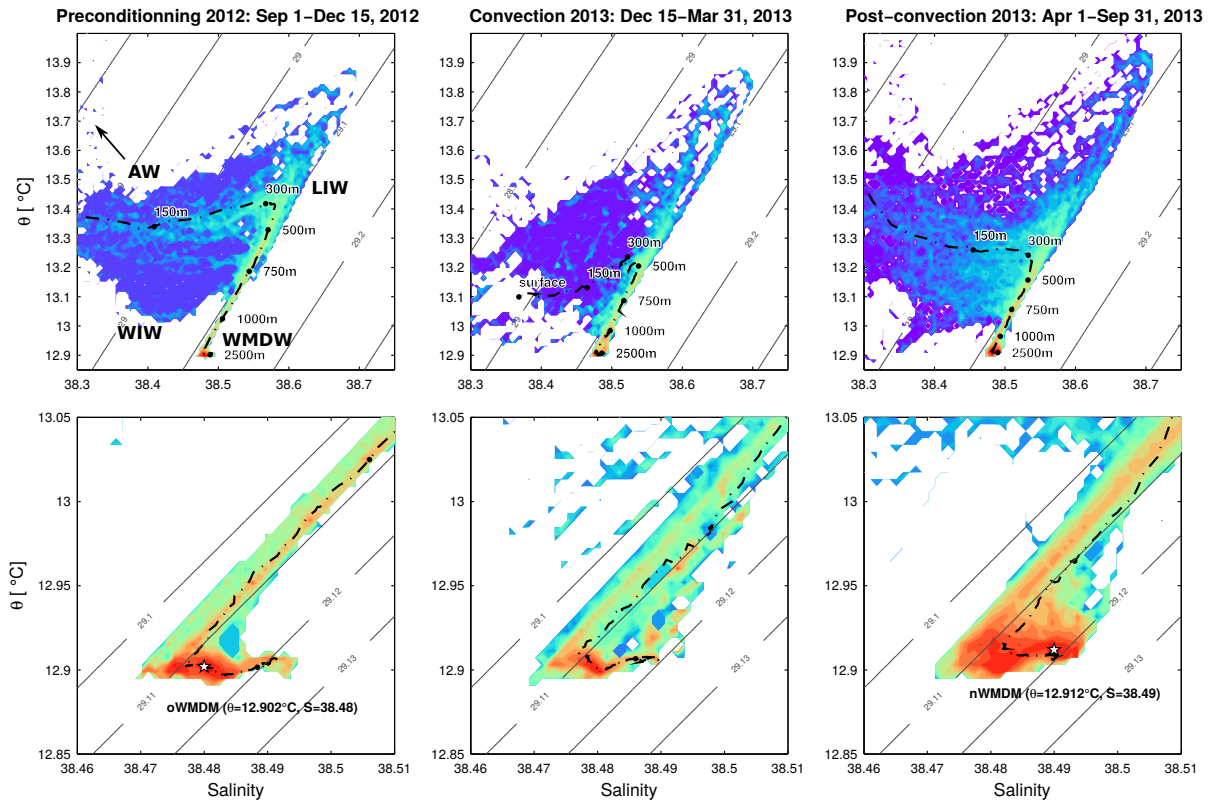


Figure 3. Probability density function in the θ/S space of all CTD casts data during the MOOSE-GE 2013, DOWEX 2012, HyMeX-SOP1 2012, HyMeX SOP2 2013, DEWEX 2013-1, DEWEX 2013-2, MOOSE-GE 2013, and DOWEX 2013 cruises, the 1% less frequent values being not shown. The dashed lines with depth labels represent the mean θ/S profile over each time period. The bottom panels focus on the deep waters and show the transformation of the deep waters during the convection event.

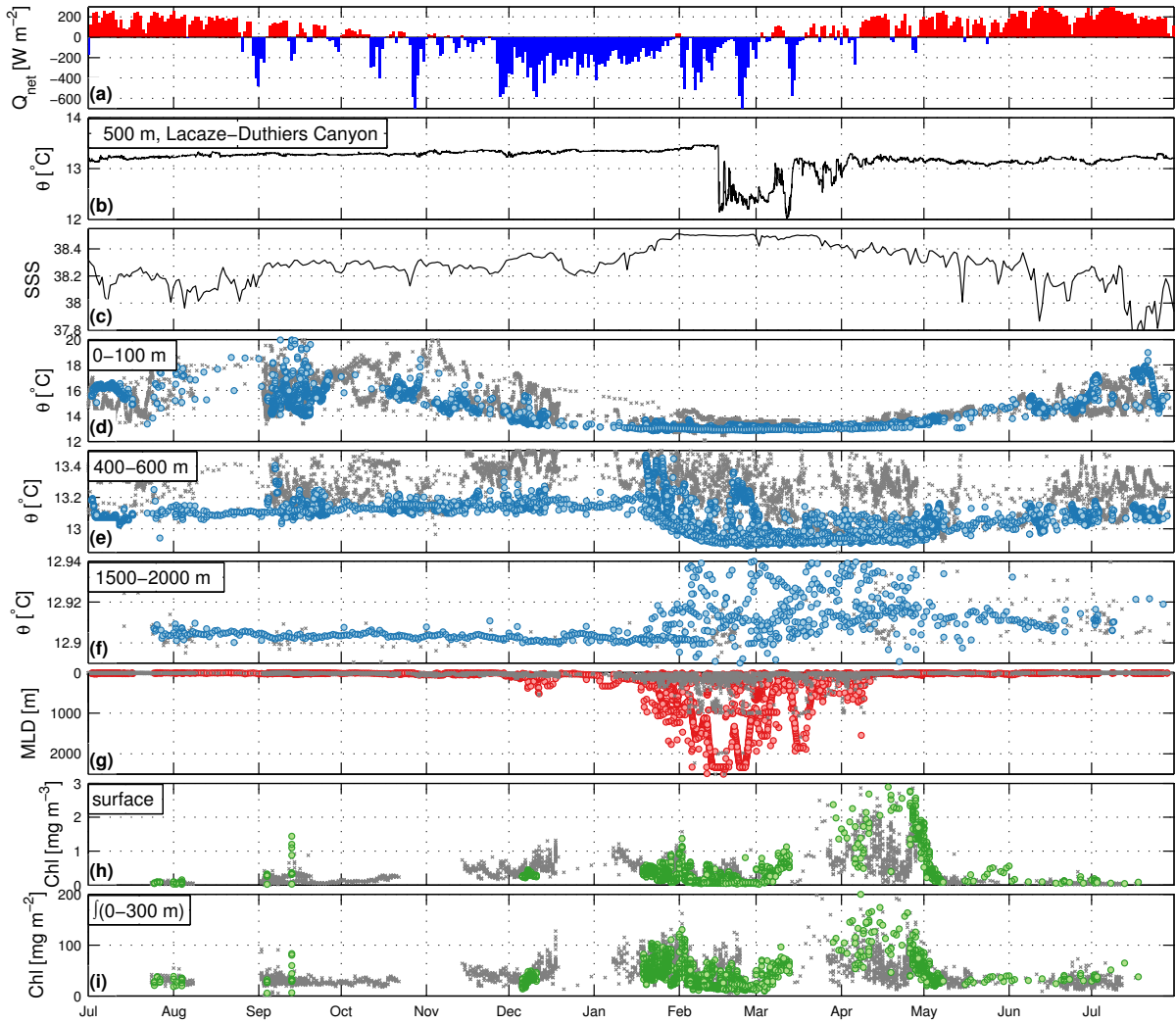


Figure 4. Timeseries of: (a) Estimated net heat fluxes at the LION buoy; (b) potential temperature at 500 m recorded in Lacaze-Duthiers canyon (Gulf of Lions shelf); (c) sea surface salinity at the LION buoy; (d) potential temperature average over the layer 0–100 m; (e) potential temperature averaged over the layer 400–600 m; (f) potential temperature average over the layer 1500–2000 m; (g) Mixed Layer Depth (MLD) estimates as in *Houpert et al.* [2016]; (h) estimates of chl-a at surface; and (i) estimates of chl-a integrated over 0–300 m. Light colors correspond to the “Boundary Current” selection area while darker colors correspond to the “Mixed Patch” one (see white delineated areas on Figure 1).

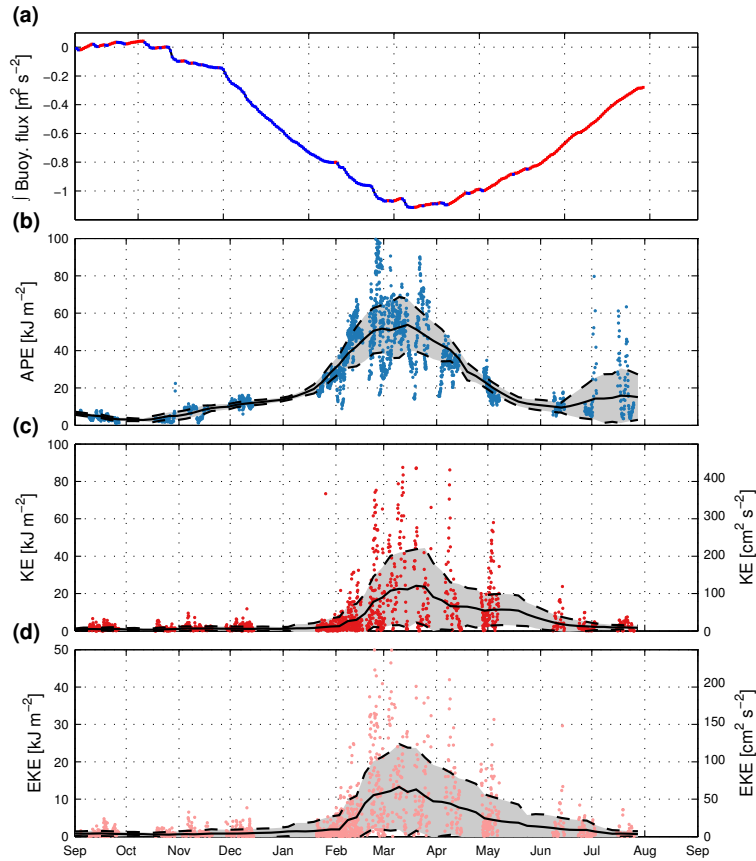


Figure 5. Timeseries of: (a) Integrated buoyancy flux estimated at the LION meteorological buoy (blue dots indicate negative net heat flux, and red positive ones); (b) Available Potential Energy (APE) integrated from the surface down to 1000 m from all glider density profiles; (c) total Kinetic Energy (KE); and (d) Eddy Kinetic Energy (EKE) estimated for 0–1000 m layer from the glider depth-average currents. The black line shows the mean signal binned into 5 days period and smoothed with a moving average of 30 days. The gray shaded area represents the standard deviation in each 5 days bin.

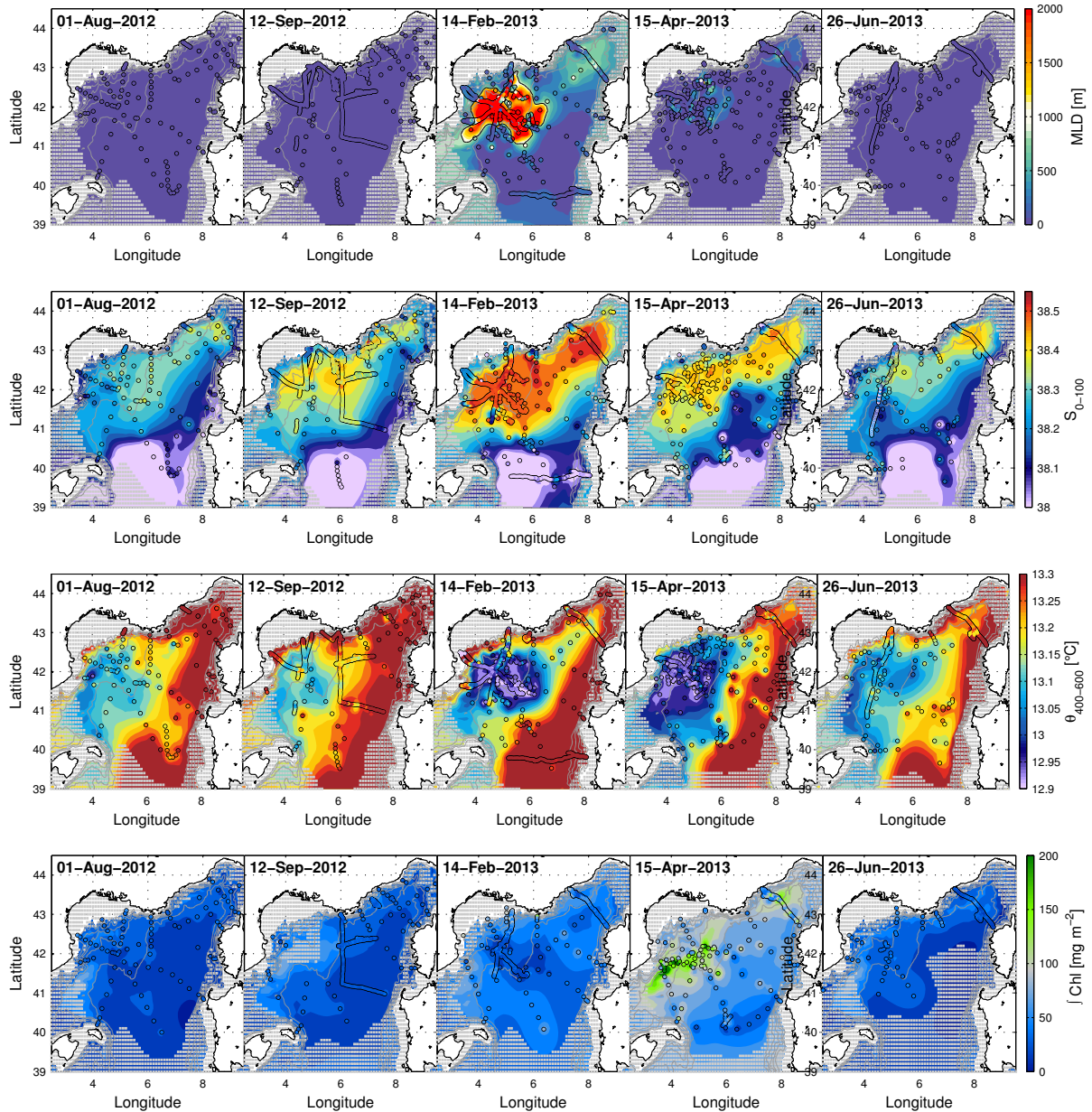


Figure 6. Objective analyses of a) MLD estimates as in [Houpert et al., 2016], homogeneous profiles over more than 1000m were extrapolated to the bottom along the vertical thanks to LION mooring data b) surface Salinity (averaged over 0–100 m), c) potential temperature at intermediate depth (averaged over 400–600 m), d) chl-a estimates averaged over 0–300 m. Extrapolated values being estimated to have an error of more than 95% in terms of variance of the analyzed field at 75km are shaded. Data points within 10 days from the date of the analysis are superimposed (in black circles filled with A F T colors coded with values).

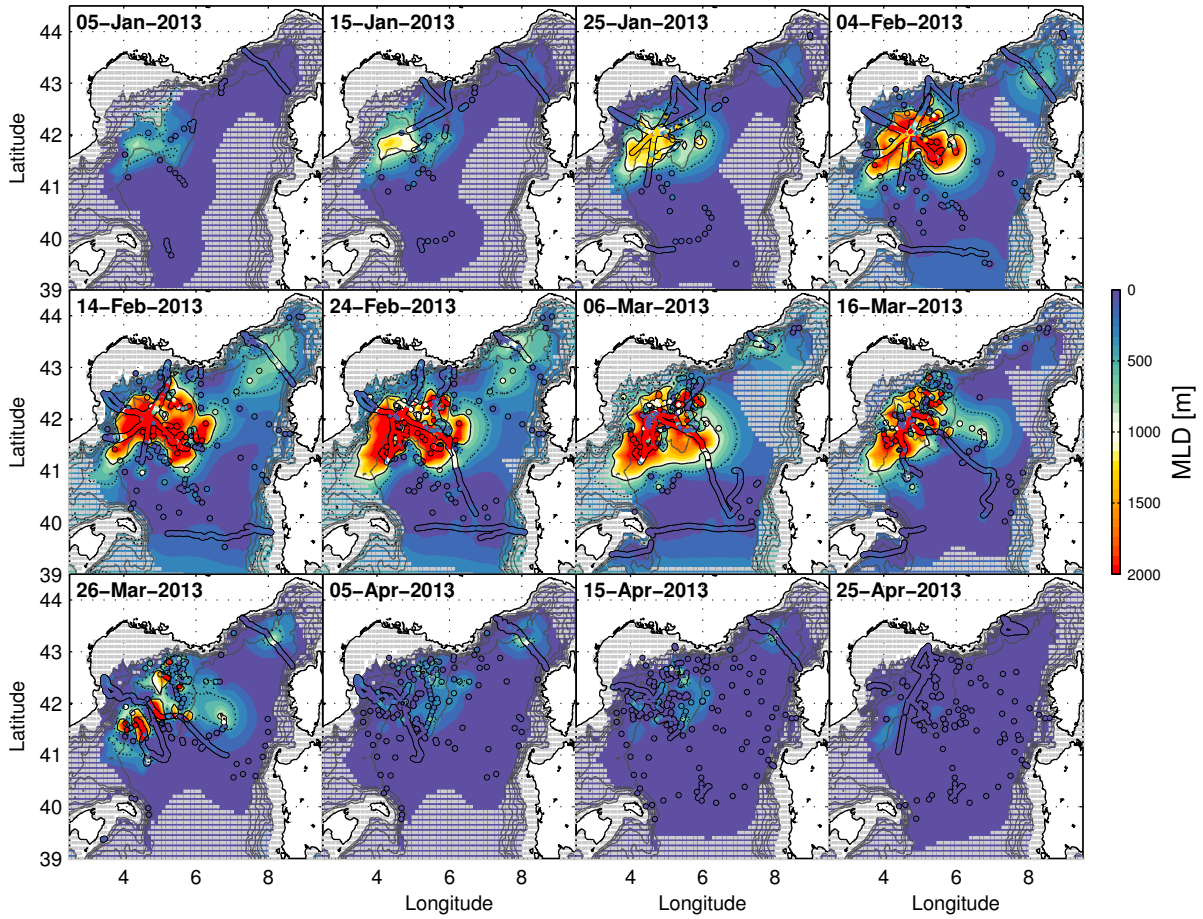


Figure 7. Objective analysis of MLD similar as in figure 6 computed on a 10-day basis. Continuous and dashed black contours indicate MLD greater than 1000m and 500m respectively.

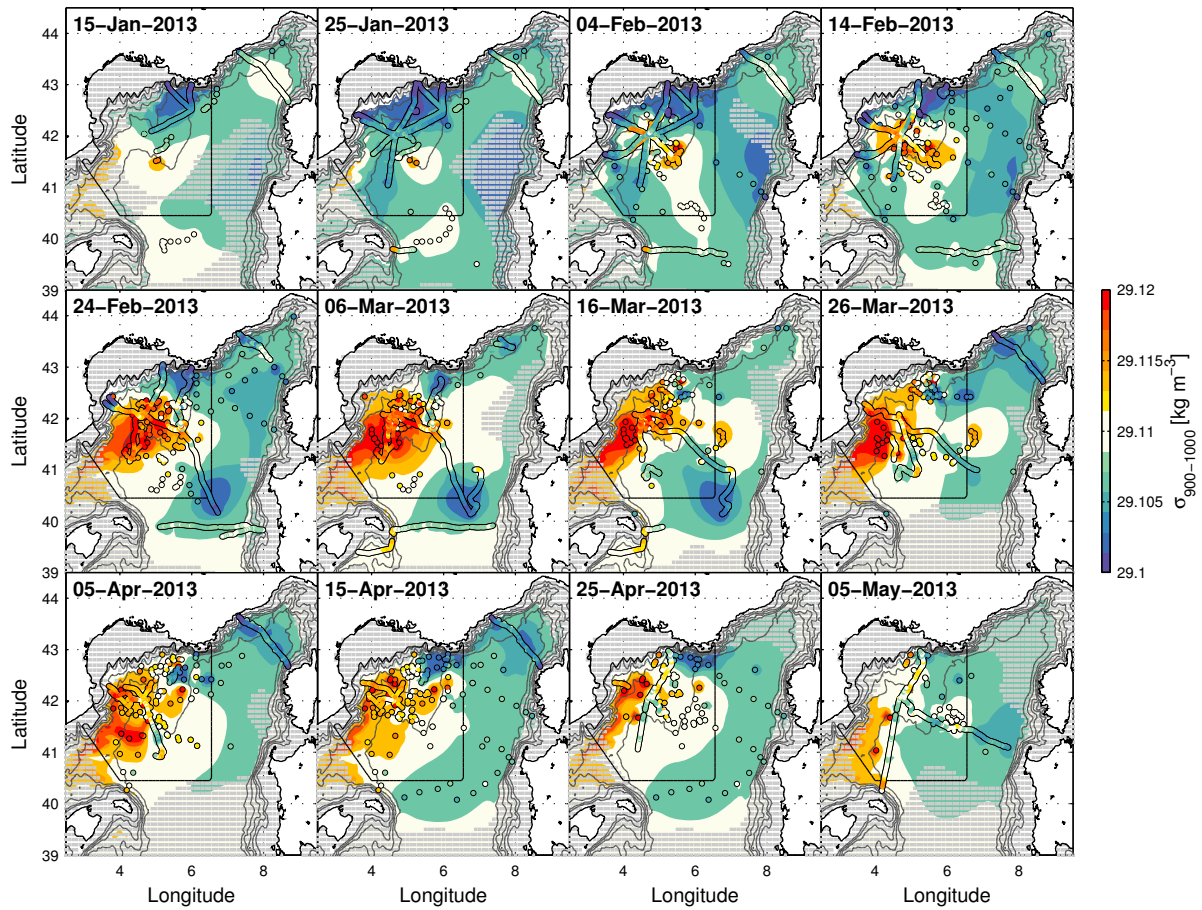


Figure 8. Objective analysis of potential density averaged over 900-1000m depth on a 10-day basis. The convection area used to assess deep water formation rates is delineated in black.

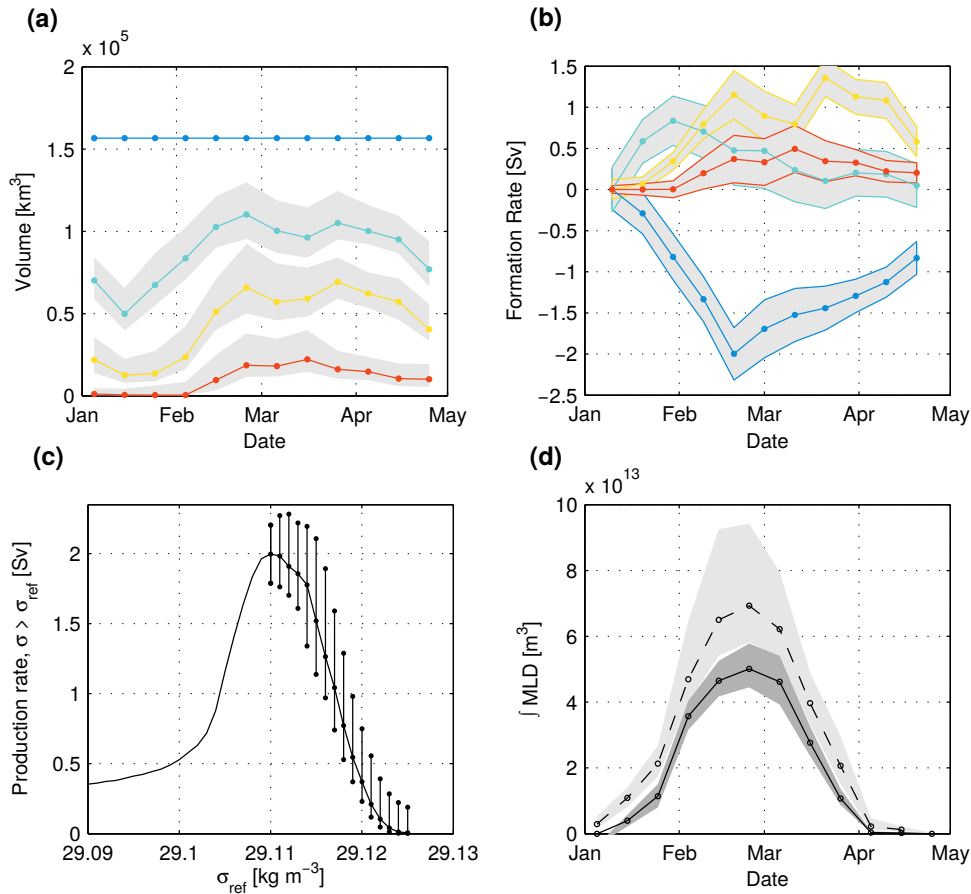


Figure 9. (a) Temporal evolution of the volume for waters presenting greater densities than 28.3 kg/m^3 (blue) corresponding to the minimum density observed in the deep convection area shown in figure 8, 29.11 kg/m^3 (green), 29.115 kg/m^3 (yellow) and 29.12 kg/m^3 (red). Error bars in gray result from the optimal interpolation error. (b) Temporal evolution of the volume of water between consecutive isopycnals calculated by comparison to the situation on 5th January and reduced to Sv (volume averaged over one year) for waters presenting densities lower than 29.11 kg/m^3 (blue), between 29.11 kg/m^3 and 29.15 kg/m^3 (green), between 29.115 kg/m^3 and 29.12 kg/m^3 (yellow) and greater than 29.12 kg/m^3 (red). Error bars result from those of panel (a). (c) Volume of water denser than a given isopycnal produced between the 5th January and 24th of February. Error bars are computed from the volume error of each density class of the optimal interpolation. For clarity, they are only plotted for waters undergoing a net volume increase during

December-February period. (d) Convective October 23, 2017, to 16 January 2018. The continuous line represents this quantity for MLD greater than 1000 m, the dashed line for MLD greater than 500 m. Error bars in gray result from the optimal interpolation error.

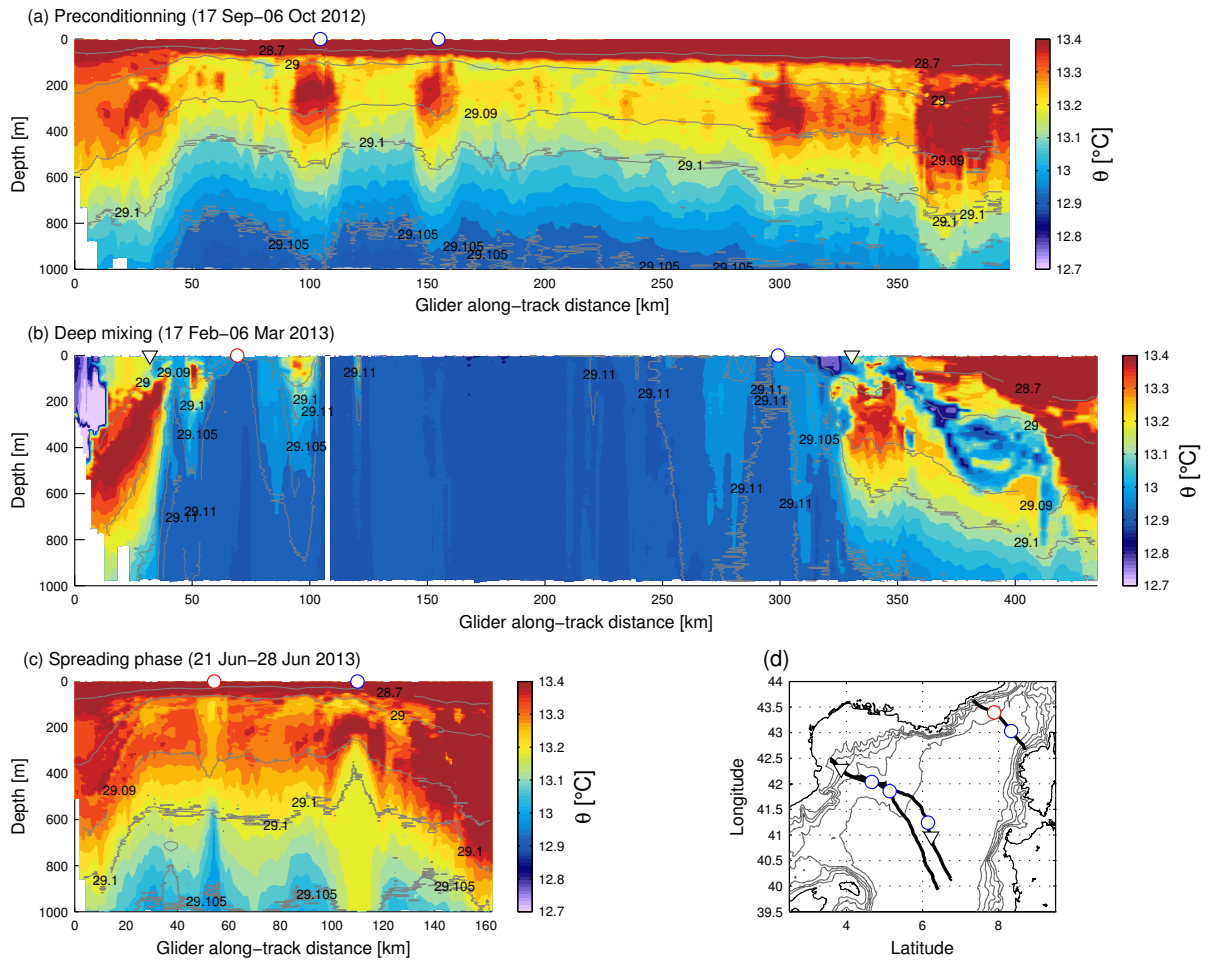


Figure 10. Glider potential temperature sections across the northwestern basin illustrating the role of SCVs during the (a) preconditioning, (b) violent mixing and (c) spreading phases. White circles indicate locations of SCVs. White triangles indicate interleaving at the edge of the deep convection area.

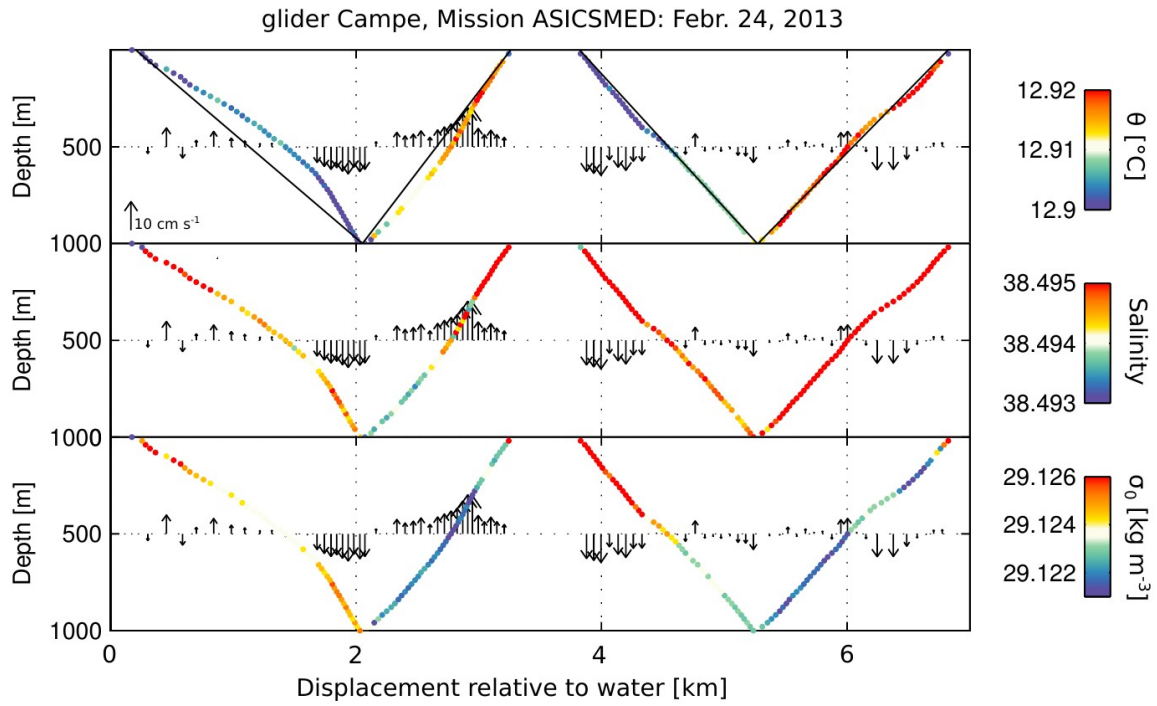


Figure 11. Vertical trajectory of a glider evolving in the *Mixed Patch* during violent mixing events color-coded with potential temperature, salinity and potential density and estimates (black arrows) of oceanic vertical velocities based on the glider flight model presented in *Margirier et al.*

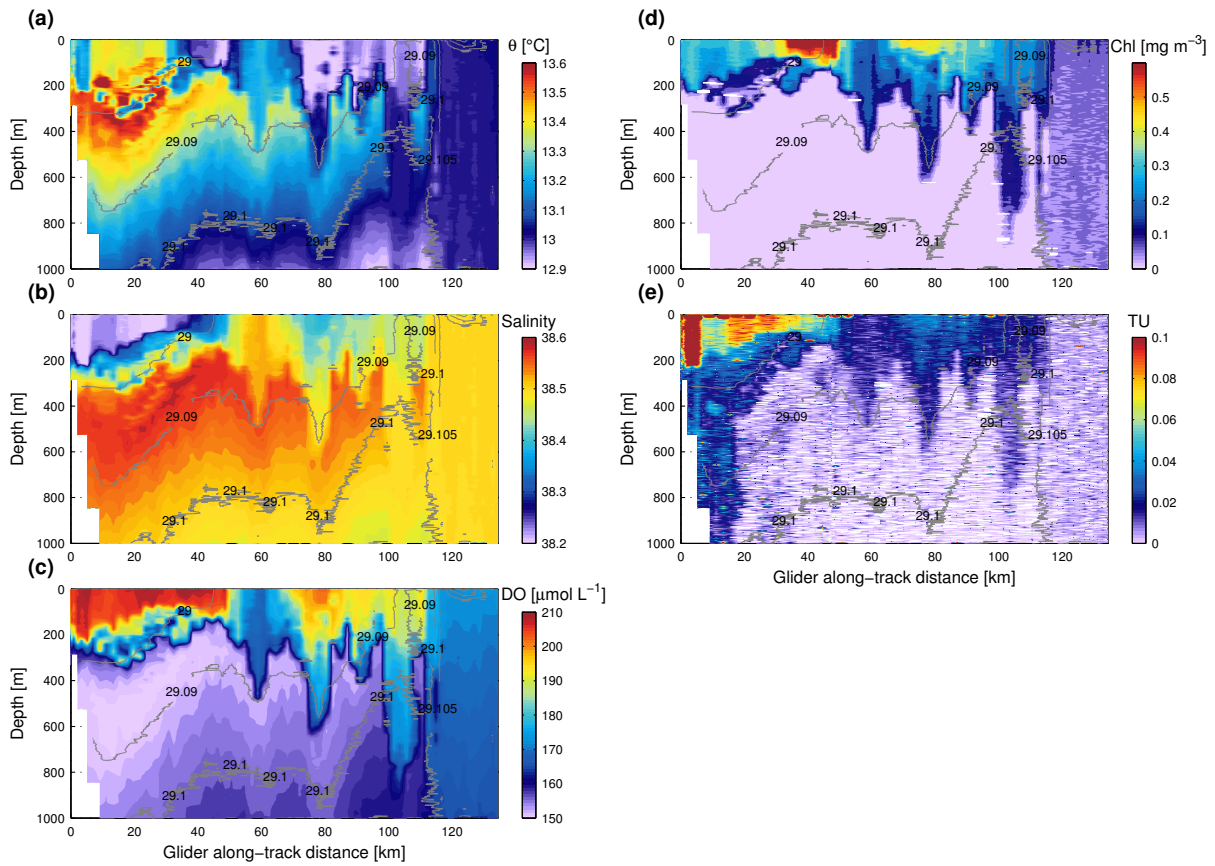


Figure 12. Glider sections across the *Transition Zone* between the Northern Current and the *Mixed Patch* of a) potential temperature, b) salinity, c) dissolved oxygen (uncalibrated), d) chl-a fluorescence and e) turbidity (uncalibrated).

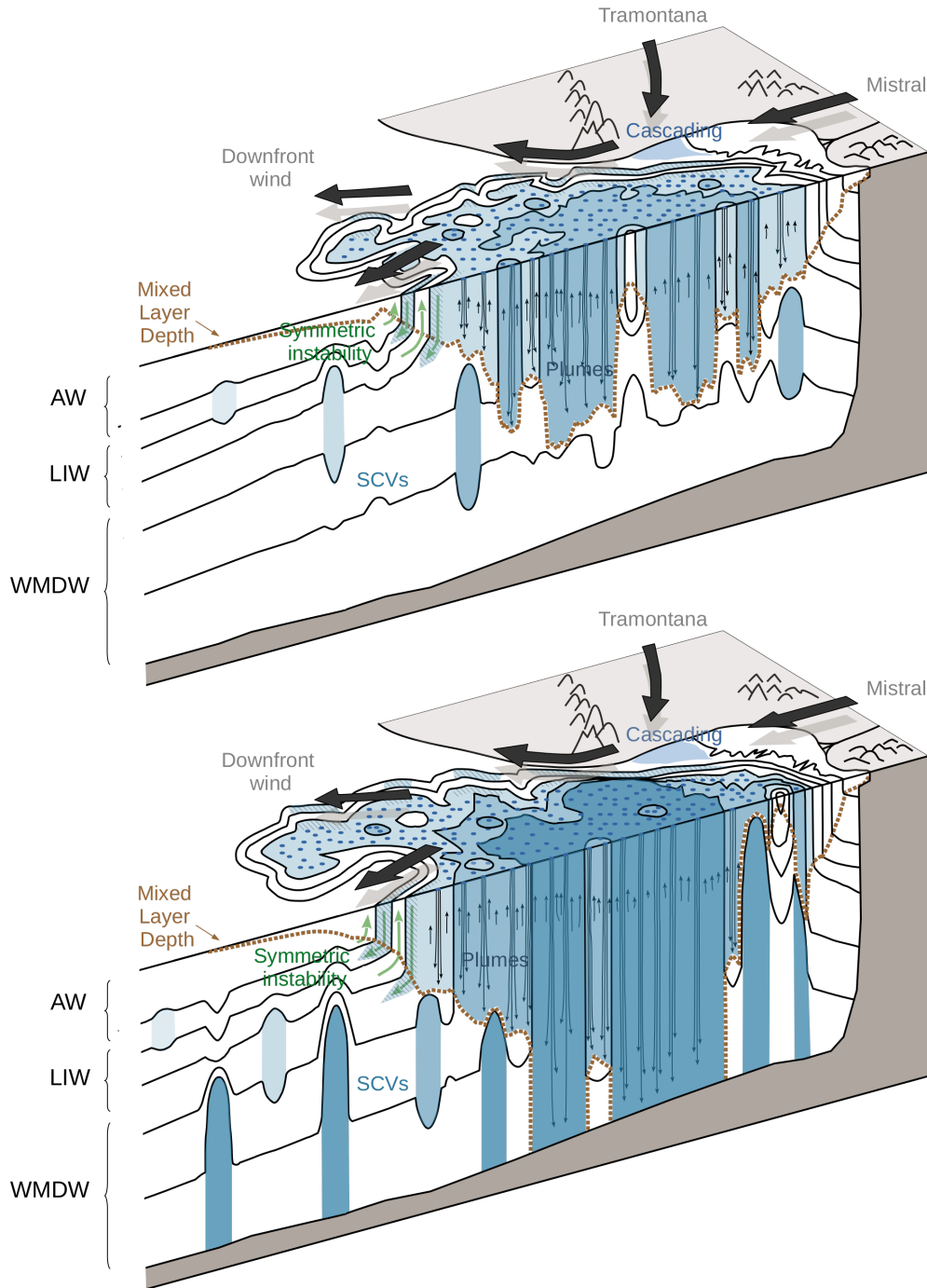


Figure 13. Schematic diagram of the evolution of the convection area during the violent mixing phase in a period of 1-2 weeks. Underlying stratification/outcrop is shown by selected isopycnals (continuous black lines). The volume of fluid just mixed by convection is shaded and color coded according to potential density classes.

1175 **Acknowledgments.** Hydrographical data were collected, and made freely available by the
1176 Coriolis project (<http://www.coriolis.eu.org>) and programmes that contribute. We would like to
1177 acknowledge the staff of the French National Pool of Gliders (DT-INSU/CNRS-CETSM/Ifremer)
1178 for the sustained gliders deployments carried out in the framework of MOOSE, as well as the
1179 intensive deployments during this 2012-2013 DEWEX experiment and to warmly thank Captains
1180 and crews of R/V *Le Tethys II* (CNRS/INSU, France), R/V *Le Provence* (Phares et Balises,
1181 France), and R/V *Le Suroît* (Ifremer, France) and R/V *Urania* (CNR, Italy), as well as all sci-
1182 entists, engineers, technicians and students who participated to the MOOSE-GE, HyMeX/SOP1
1183 and SOP2, DEWEX, and DOWEX different cruises and autonomous platforms deployments.
1184 Support was provided by the French "Chantier Méditerranée" MISTRALS program (HyMeX and
1185 MERMeX components), the ANR ASICSMED project (ANR 12-BS06-0003), the MOOSE long-
1186 term observatory (SOERE/AllEnvi-SNO/INSU), the Bio-Argo project (CNES-TOSCA) and the
1187 ANR NAOS project (ANR J11R107F), as well as the NATO STO-CMRE NOMR12 experiment.
1188 Support was also provided by the EU projects FP7 GROOM (Grant Agreement No. 284321),
1189 FP7 PERSEUS (Grant Agreement No. 287600), FP7 JERICO (Grant Agreement No. 262584)
1190 and the COST Action ES0904 "EGO" (Everyone's Gliding Observatories).

1191

References

- 1192 Adloff, F., et al. (2015), Mediterranean Sea response to climate change in an ensemble of twenty
1193 first century scenarios, *Climate Dynamics*, doi:10.1007/s00382-015-2507-3.
- 1194 Auger, P., C. Ulses, C. Estournel, L. Stemman, S. Somot, and F. Diaz (2014), Interannual control
1195 of plankton ecosystem in a deep convection area as inferred from a 30-year 3d modeling study:

- 1196 winter mixing and prey/predator in the nw mediterranean., *Progress in Oceanography*, 12-27.
- 1197 Béthoux, J.-P., X. Durieu de Madron, F. Nyffeler, and D. Tailliez (2002), Deep water in the
1198 western Mediterranean: Peculiar 1999 and 2000 characteristics, shelf formation hypothesis,
1199 variability since 1970 and geochemical inferences, *Journal of Marine Systems*, 33-34, 117–131,
1200 doi:10.1016/S0924-7963(02)00055-6.
- 1201 Boehme, L., and U. Send (2005), Objective analyses of hydrographic data for referencing profiling
1202 float salinities in highly variable environments, *Deep Sea Research Part II: Topical Studies in*
1203 *Oceanography*, 52(3-4), 651–664, doi:10.1016/j.dsr2.2004.12.014.
- 1204 Bosse, A. (2015), Circulation générale et couplage physique-biogéochimie à (sous-)mésoséchelle
1205 en Méditerranée Nord-occidentale à partir de données in situ, Ph.D. thesis, Université Pierre
1206 et Marie Curie, Paris.
- 1207 Bosse, A., P. Testor, L. Mortier, L. Prieur, V. Taillandier, F. D’Ortenzio, and L. Coppola (2015),
1208 Spreading of Levantine Intermediate Waters by submesoscale coherent vortices in the north-
1209 western Mediterranean Sea as observed with gliders, *Journal of Geophysical Research: Oceans*,
1210 120, 1599–1622, doi:10.1002/2014JC010263.
- 1211 Bosse, A., et al. (2016), Scales and dynamics of submesoscale coherent vortices formed by deep
1212 convection in the northwestern mediterranean sea, *Journal of Geophysical Research: Oceans*,
1213 121(10), 7716–7742, doi:10.1002/2016JC012144.
- 1214 Bosse, A., et al. (2017), A submesoscale coherent vortex in the ligurian sea: From dynamical
1215 barriers to biological implications, *Journal of Geophysical Research: Oceans*, 122(8), 6196–
1216 6217, doi:10.1002/2016JC012634.
- 1217 Bouin, M.-N., and J. Rolland (2011), Lion mto-france buoy 0-250 m ocean tem-
1218 perature mooring line, pyranometer and pyrgeometer, sea surface tempera-

- 1219 ture and salinity, *Tech. rep.*, doi:[https://doi.org/10.6096/MISTRALS-HyMeX-](https://doi.org/10.6096/MISTRALS-HyMeX-MOOSE.388)
1220 MOOSE.388; <https://doi.org/10.6096/HyMeX.LionBuoy.Pyranometer.20100308>;
1221 <https://doi.org/10.6096/MISTRALS-HyMeX-MOOSE.1025>.
- 1222 Cacho, I., J. Grimalt, and M. Canals (2002), Response of the western mediterranean sea to rapid
1223 climatic variability during the last 50,000 years: a molecular biomarker approach, *Journal of*
1224 *Marine Systems*, *33*, 253-272.
- 1225 Caniaux, G., L. Prieur, H. Giordani, and J.-L. Redelsperger (2017), An inverse method to derive
1226 surface fluxes from the closure of oceanic heat and water budgets: Application to the north-
1227 western mediterranean sea, *Journal of Geophysical Research: Oceans*, *122*(4), 2884–2908, doi:
1228 [10.1002/2016JC012167](https://doi.org/10.1002/2016JC012167).
- 1229 Coll, M., et al. (2010), The biodiversity of the mediterranean sea: Estimates, patterns, and
1230 threats., *PLoS ONE*, *5*(8), doi:<https://doi.org/10.1371/journal.pone.0011842>.
- 1231 Conan, P. (2013), DEWEX-MERMEX 2013 LEG2 cruise, RV Le Suroît, *Tech. rep.*, doi:
1232 [10.17600/13020030](https://doi.org/10.17600/13020030).
- 1233 Conan, P., et al. (2007), Partitioning of organic production in marine plankton communities:
1234 The effects of inorganic nutrient ratios and community composition on new dissolved organic
1235 matter, *Limnol. Oceanogr.*, *52*(2), 753-765.
- 1236 Coppola, L., L. Prieur, I. Taupier-Letage, C. Estournel, P. Testor, D. Lefevre, S. Belamari,
1237 S. LeReste, and V. Taillandier (2017), Observation of oxygen ventilation into deep wa-
1238 ters through targeted deployment of multiple argo-o2 floats in the north-western mediter-
1239 ranean sea in 2013, *Journal of Geophysical Research: Oceans*, *122*(8), 6325–6341, doi:
1240 [10.1002/2016JC012594](https://doi.org/10.1002/2016JC012594).

- 1241 Damien, P., A. Bosse, P. Testor, P. Marsaleix, and C. Estournel (2017), Modeling postconvective
1242 submesoscale coherent vortices in the northwestern mediterranean sea, *Journal of Geophysical*
1243 *Research: Oceans*, pp. n/a–n/a, doi:10.1002/2016JC012114.
- 1244 D’Ortenzio, F., et al. (2014), Observing mixed layer depth, nitrate and chlorophyll concentrations
1245 in the northwestern Mediterranean: A combined satellite and NO₃ profiling floats experiment,
1246 *Geophysical Research Letters*, *41*(18), 6443–6451, doi:10.1002/2014GL061020.
- 1247 Ducrocq, V., et al. (2014), Hymex-sop1, the field campaign dedicated to heavy precipitation and
1248 flash-flooding in the northwestern mediterranean, *Bull. Amer. Meteor. Soc.*, *95*, 10831100,
1249 doi:http://dx.doi.org/10.1175/BAMS-D-12-00244.1.
- 1250 Durrieu de Madron, X., et al. (2011), Marine ecosystems’ responses to climatic and an-
1251 thropogenic forcings in the Mediterranean, *Progress in Oceanography*, *91*(2), 97–166, doi:
1252 10.1016/j.pocean.2011.02.003.
- 1253 Durrieu de Madron, X., et al. (2013), Interaction of dense shelf water cascading and open-
1254 sea convection in the northwestern Mediterranean during winter 2012, *Geophysical Research*
1255 *Letters*, *40*(7), 1379–1385, doi:10.1002/grl.50331.
- 1256 Durrieu de Madron, X., et al. (2017), Deep sediment resuspension and generation and thick
1257 nepheloid layer generation by open-ocean convection, *Journal of Geophysical Research: Oceans*,
1258 *122*, doi:doi:10.1002/2016JC012062.
- 1259 Estournel, C., et al. (2016a), Hymex-sop2: The field campaign dedicated to dense water forma-
1260 tion in the northwestern mediterranean, *Oceanography*, *29*, [ip1](#)The HYdrological cycle in the
1261 Mediterranean Experiment (HyMeX) Special Observing Period 2 (SOP2, January 27March
1262 15, 2013) was dedicated to the study of dense water formation in the Gulf of Lion in the
1263 northwestern Mediterranean. This paper outlines the deep convection of winter 20122013 and

1264 the meteorological conditions that produced it. Alternating phases of mixing and restratifica-
1265 tion are related to periods of high and low heat losses, respectively. High-resolution, realistic,
1266 three-dimensional models are essential for assessing the intricacy of buoyancy fluxes, horizon-
1267 tal advection, and convective processes. At the submesoscale, vertical velocities resulting from
1268 symmetric instabilities of the density front bounding the convection zone are crucial for venti-
1269 lating the deep ocean. Finally, concomitant atmospheric and oceanic data extracted from the
1270 comprehensive SOP2 data set highlight the rapid, coupled evolution of oceanic and atmospheric
1271 boundary layer characteristics during a strong wind event.

1272 Estournel, C., et al. (2016b), High resolution modeling of dense water formation in the north-
1273 western mediterranean during winter 20122013: Processes and budget, *Journal of Geophysical*
1274 *Research: Oceans*, *121*(7), 5367–5392, doi:10.1002/2016JC011935.

1275 Fairall, C., E. Bradley, J. Hare, A. Grachev, and J. Edson (2003), Bulk parameterization of
1276 air-sea fluxes: Updates and verification for the coare algorithm., *J. Clim.*, *16*: 571591.

1277 Garau, B., S. Ruiz, W. G. Zhang, A. Pascual, E. E. Heslop, J. Kerfoot, and J. Tintoré (2011),
1278 Thermal Lag Correction on Slocum CTD Glider Data, *Journal of Atmospheric and Oceanic*
1279 *Technology*, *28*(9), 1065–1071, doi:10.1175/JTECH-D-10-05030.1.

1280 Gascard, J.-C. (1978), Mediterranean deep water formation baroclinic instability and oceanic
1281 eddies, *Oceanologica Acta*, *1*(3), 315–330.

1282 Gascard, J.-c., A. J. Watson, M.-J. Messias, K. A. Olsson, T. Johannessen, and K. Simonsen
1283 (2002), Long-lived vortices as a mode of deep ventilation in the Greenland Sea, *Nature*, *416*,
1284 525–527.

1285 Gieskes, W. W., , and K. G. W. (1983), Unknown chlorophyll a derivatives in the north sea and
1286 the tropical atlantic ocean revealed by hplc analysis., *Limnol. Oceanogr.*, *28*: 757-766.

- 1287 Giordani, H., C. Lebeaupin-Brossier, F. Lger, and G. Caniaux (2017), A pv-approach for dense
1288 water formation along fronts: Application to the northwestern mediterranean, *Journal of Geo-*
1289 *physical Research: Oceans*, 122(2), 995–1015, doi:10.1002/2016JC012019.
- 1290 Giorgi, F. (2006), Climate change hotspots., *Geophysical research letters*, 33(8).
- 1291 Herrmann, M., C. Estournel, F. Adloff, and F. Diaz (2014), Impact of climate change on the
1292 northwestern {Mediterranean} {Sea} pelagic planktonic ecosystem and associated carbon cy-
1293 cle, *Journal of Geophysical Research: Oceans*, 119(9), 5815–5836, doi:10.1002/2014JC010016.
- 1294 Herrmann, M., P.-A. Auger, C. Ulses, and C. Estournel (2017), Long-term monitoring of ocean
1295 deep convection using multisensors altimetry and ocean color satellite data, *Journal of Geo-*
1296 *physical Research: Oceans*, 122(2), 1457–1475, doi:10.1002/2016JC011833.
- 1297 Herrmann, M. J., and S. Somot (2008), Relevance of ERA40 dynamical downscaling for
1298 modeling deep convection in the Mediterranean Sea, *Geophysical Research Letters*, 35, doi:
1299 10.1029/2007GL032442.
- 1300 Herrmann, M. J., F. Diaz, C. Estournel, P. Marsaleix, and C. Ulses (2013), Impact of atmospheric
1301 and oceanic interannual variability on the Northwestern Mediterranean Sea pelagic planktonic
1302 ecosystem and associated carbon cycle, *Journal of Geophysical Research: Oceans*, 118, 5792–
1303 5813, doi:10.1002/jgrc.20405.
- 1304 Houpert, L. (2013), Contribution to the Study of Transfer Processes from the Surface to the
1305 Deep Ocean in the Mediterranean Sea using in situ Measurements, Ph.D. thesis, Université de
1306 Perpignan.
- 1307 Houpert, L., et al. (2016), Observations of open-ocean deep convection in the northwest-
1308 ern mediterranean sea: Seasonal and interannual variability of mixing and deep water
1309 masses for the 20072013 period, *Journal of Geophysical Research: Oceans*, pp. n/a–n/a, doi:

1310 10.1002/2016JC011857.

1311 Jones, H., and J. Marshall (1997), Restratification after Deep Convection, *Journal of Physical*
1312 *Oceanography*, *27*, 2276–2287, doi:10.1175/1520-0485(1997)027<2276:RADC>2.0.CO;2.

1313 Killworth, P. (1976), The mixing and spreading phase of medoc 1969, *Progr. Oceanogr.*, *7*, 59-90.

1314 Killworth, P. (1979), On “chimney” formation in the ocean, *J. Phys. Oceanogr.*, *9*, 531-5547,
1315 59-90.

1316 Lavigne, H., F. D’Ortenzio, H. Claustre, and A. Poteau (2012), Towards a merged satellite and in
1317 situ fluorescence ocean chlorophyll product, *Biogeosciences*, *9*(6), 2111–2125, doi:10.5194/bg-
1318 9-2111-2012.

1319 Lavigne, H., F. D’Ortenzio, C. Migon, H. Claustre, P. Testor, M. Ribera d’Alcalà, R. Lavezza,
1320 L. Houpert, and L. Prieur (2013), Enhancing the comprehension of mixed layer depth control
1321 on the Mediterranean phytoplankton phenology, *Journal of Geophysical Research: Oceans*,
1322 *118*, 3416–3430, doi:10.1002/jgrc.20251.

1323 Le Traon, P. Y. (1990), A method for optimal analysis of fields with spatially variable mean, *J.*
1324 *Geophys. Res.*, *95*, Issue C8, Pages 1354313547, doi:10.1029/JC095iC08p13543.

1325 Lebeaupin-Brossier, C., et al. (2014), Ocean mixed layer responses to intense
1326 meteorological events during hymex-sop1 from a high-resolution ocean simula-
1327 tion, *Ocean Modelling*, *84*, December 2014, Pages 84-103, ISSN 1463-5003, doi:
1328 <http://dx.doi.org/10.1016/j.ocemod.2014.09.009>.

1329 Legg, S., and J. C. Marshall (1993), A Heton Model of the Spreading Phase of Open-
1330 Ocean Deep Convection, *Journal of Physical Oceanography*, *23*, 1040–1056, doi:10.1175/1520-
1331 0485(1993)023;1040:AHMOTS;2.0.CO;2.

- 1332 Legg, S., and J. C. McWilliams (2001), Convective Modifications of a Geostrophic
1333 Eddy Field, *Journal of Physical Oceanography*, *31*, 874–891, doi:10.1175/1520-
1334 0485(2001)031;0874:CMOAGE;2.0.CO;2.
- 1335 Legg, S., J. McWilliams, and J. Gao (1998), Localization of Deep Ocean Convection
1336 by a Mesoscale Eddy, *Journal of Physical Oceanography*, *28*, 944–970, doi:10.1175/1520-
1337 0485(1998)028<0944:LODOCB>2.0.CO;2.
- 1338 ”L’Hévéder, B., L. Li, F. Sevault, and S. Somot (2013), Interannual variability of deep convection
1339 in the northwestern mediterranean simulated with a coupled aorcm, *Climate Dynamics*, *41*(3),
1340 937–960, doi:10.1007/s00382-012-1527-5.
- 1341 Lilly, J. M., P. B. Rhines, M. Visbeck, R. E. Davis, J. R. N. Lazier, F. Schott,
1342 and D. Farmer (1999), Observing Deep Convection in the Labrador Sea during
1343 Winter 1994/95, *Journal of Physical Oceanography*, *29*, 2065–2098, doi:10.1175/1520-
1344 0485(1999)029;2065:ODCITL;2.0.CO;2.
- 1345 Lger, F., et al. (2016), Dense water formation in the north-western mediterranean area during
1346 hymex-sop2 in 1/36 ocean simulations: Sensitivity to initial conditions, *Journal of Geophysical*
1347 *Research: Oceans*, *121*(8), 5549–5569, doi:10.1002/2015JC011542.
- 1348 Madec, G., M. Chartier, P. Delecluse, and M. Crépon (1991), A three-dimensional numerical
1349 study of deep-water formation in the northwestern Mediterranean Sea, *Journal of Physical*
1350 *Oceanography*, *21*, 1349–1371.
- 1351 Mahadevan, A. (2006), Modeling vertical motion at ocean fronts: Are nonhydrostatic effects rele-
1352 vant at submesoscales?, *Ocean Modelling*, *14*(3-4), 222–240, doi:10.1016/j.ocemod.2006.05.005.
- 1353 Margirier, F., A. Bosse, P. Testor, B. L’Hvder, L. Mortier, and D. Smeed (), Characterization of
1354 convective plumes associated with oceanic deep convection in the northwestern mediterranean

- 1355 from high resolution in-situ data collected by gliders, *Journal of Geophysical Research: Oceans*,
1356 pp. n/a–n/a, doi:10.1002/2016JC012633.
- 1357 Marshall, J., and F. Schott (1999), Open-ocean convection: Observations, theory, and models,
1358 *Reviews of Geophysics*, *37*(1), 1–64, doi:10.1029/98RG02739.
- 1359 Mayot, N., F. D’Ortenzio, V. Taillandier, L. Prieur, O. Pasqueron de Fommervault, H. Claus-
1360 tre, A. Bosse, P. Testor, and P. Conan (2017), Physical and biogeochemical controls of the
1361 phytoplankton blooms in north-western mediterranean sea: A multiplatform approach over a
1362 complete annual cycle (20122013 dewex experiment), *Journal of Geophysical Research: Oceans*,
1363 pp. n/a–n/a, doi:10.1002/2016JC012052.
- 1364 McWilliams, J. C. (1985), Submesoscale, coherent vortices in the ocean, *Reviews of Geophysics*,
1365 *23*(2), 165, doi:10.1029/RG023i002p00165.
- 1366 MEDOC-Group, T. (1970), Observation of Formation of Deep Water in the Mediterranean Sea,
1367 1969, *Nature*, *225*, 1037–1040, doi:10.1038/2271037a0.
- 1368 Mortier, L. (2012), DOWEX2012 cruise, RV Téthys II, *Tech. rep.*, doi:10.17600/12450170.
- 1369 Mortier, L., and V. Taillandier (2013), DOWEX2013 cruise, RV Téthys II, *Tech. rep.*, doi:
1370 10.17600/13450150.
- 1371 Pasqueron de Fommervault, O., et al. (2015), Seasonal variability of nutrient concentrations
1372 in the mediterranean sea: Contribution of bio-argo floats, *Journal of Geophysical Research:*
1373 *Oceans*, *120*(12), 8528–8550, doi:10.1002/2015JC011103.
- 1374 Pusceddu, A., et al. (2010), Ecosystems effects of dense water formation on deep mediterranean
1375 sea ecosystems : an overview., *Advances in Oceanography and Limnology*, *1*, *1*, 67-83.
- 1376 Schott, F., and K. D. Leaman (1991), Observations with Moored Acoustic Doppler
1377 Current Profilers in the Convection Regime in the Golfe du Lion, doi:10.1175/1520-

1378 0485(1991)021;0558:OWMADC;2.0.CO;2.

1379 Schott, F., M. Visbeck, U. Send, J. Fischer, L. Stramma, and Y. Desaubies (1996), Ob-
1380 servations of Deep Convection in the Gulf of Lions, Northern Mediterranean, during
1381 the Winter of 1991/92, *Journal of Physical Oceanography*, *26*, 505–524, doi:10.1175/1520-
1382 0485(1996)026;0505:OODCIT;2.0.CO;2.

1383 Send, U., and J. Marshall (1995), Integral effects of deep convection, *Journal of Physical Oceanog-*
1384 *raphy*, *25*(5), 855–872, doi:10.1175/1520-0485(1995)025<0855:IEODC>2.0.CO;2.

1385 Somot, S., F. Sevault, and M. Déqué (2006), Transient climate change scenario simulation of the
1386 Mediterranean Sea for the twenty-first century using a high-resolution ocean circulation model,
1387 *Climate Dynamics*, *27*(7-8), 851–879, doi:10.1007/s00382-006-0167-z.

1388 Somot, S., et al. (2016), Characterizing, modelling and understanding the climate variability
1389 of the deep water formation in the north-western mediterranean sea, *Climate Dynamics*, doi:
1390 10.1007/s00382-016-3295-0.

1391 Stabholz, M., et al. (2013), Impact of open-ocean convection on particle fluxes and sediment
1392 dynamics in the deep margin of the Gulf of Lions, *Biogeosciences*, *10*(2), 1097–1116, doi:
1393 10.5194/bg-10-1097-2013.

1394 Tamburini, C., M. Canals, X. Durrieu de Madron, L. Houpert, D. Lefvre, S. Martini,
1395 A. D’Ortenzio, F. and Robert, P. Testor, and et al. (2013), Deep-sea bioluminescence blooms
1396 after dense water formation at the ocean surface, *PLoS ONE*, *07/2013*, *8*(7):e67523.

1397 Taupier-Letage, I. (2013), Temperature, Salinity and Density (CTD) vertical profiles during
1398 HyMeX SOP1, *Tech. rep.*, doi:10.6096/MISTRALS-HYMEX.CTD_SOP1.20130610.

1399 Taupier-Letage, I., and C. Bachelier (2013), CTD_SOP2, Provence - Tethys 2, *Tech. rep.*, doi:
1400 10.6096/MISTRALS-HyMeX.950.

- 1401 Taupier-Letage, I., et al. (2016), Observations of wintertime surface conditions in the north-
1402 western mediterranean from the sea surface salinity (sss) and sea surface temperature (sst)
1403 transmed thermosalinograph time series (2012-2014), *J. Geophys. Res.*, *submitted, this issue*.
- 1404 Testor, P. (2013), DEWEX-MERMEX 2013 LEG1 cruise, RV Le Suroît, *Tech. rep.*, doi:
1405 10.17600/13020010.
- 1406 Testor, P., and J.-C. Gascard (2003), Large-Scale Spreading of Deep Waters in the Western
1407 Mediterranean Sea by Submesoscale Coherent Eddies, *Journal of Physical Oceanography*, *33*,
1408 75–87, doi:10.1175/1520-0485(2003)033<0075:LSSODW>2.0.CO;2.
- 1409 Testor, P., and J.-C. C. Gascard (2006), Post-convection spreading phase in the Northwestern
1410 Mediterranean Sea, *Deep Sea Research Part I*, *53*(5), 869–893, doi:10.1016/j.dsr.2006.02.004.
- 1411 Testor, P., et al. (2010), Gliders as a component of future observing systems, *Proceed-*
1412 *ings of OceanObs'09: Sustained Ocean Observations and Information for Society (Vol. 2)*,
1413 *Venice, Italy, 21-25 September 2009*, J. Hall, D.E. Harrison & D. Stammer Eds., (1), doi:
1414 10.5270/OceanObs09.cwp.89.
- 1415 Testor, P., L. Coppola, and L. Mortier (2012), MOOSE-GE 2012 cruise, RV Le Suroît, *Tech.*
1416 *rep.*, doi:10.17600/12020030.
- 1417 Testor, P., L. Coppola, and L. Mortier (2013), MOOSE-GE 2013 cruise, RV Téthys II, *Tech.*
1418 *rep.*, doi:10.17600/13450110.
- 1419 Testor, P., X. Durrieu de Madron, L. Mortier, F. d'Ortenzio, H. Legoff, D. Dausse,
1420 M. Labaste, and L. Houpert (2016), LION observatory data, SEANOE, *Tech. rep.*, doi:
1421 <http://doi.org/10.17882/44411>.
- 1422 Thomas, L. N., A. Tandon, and A. Mahadevan (2008), Sub-mesoscale processes and dynamics,
1423 *M. W. Hecht, and H. Hasumi (Eds.), Ocean Modeling in an Eddying Regime, Geophysical*

1424 *Monograph Series, 177*, 17–38, doi:10.1029/177GM04.

1425 Visbeck, M., J. Marshall, and H. Jones (1996), Dynamics of Isolated Convec-
1426 tive Regions in the Ocean, *Journal of Physical Oceanography*, doi:10.1175/1520-
1427 0485(1996)026;1721:DOICRI;2.0.CO;2.

1428 Waldman, R., et al. (), Impact of the mesoscale dynamics on ocean deep convection: The
1429 2012-2013 case study in the northwestern mediterranean sea, *Journal of Geophysical Research:*
1430 *Oceans*, pp. n/a–n/a, doi:10.1002/2016JC012587.

1431 Waldman, R., et al. (2016), Estimating dense water volume and its evolution for the year 2012–
1432 2013 in the north-western mediterranean sea: An observing system simulation experiment
1433 approach, *Journal of Geophysical Research: Oceans*, doi:10.1002/2016JC011694.

1434 Waldman, R., et al. (2017), Modeling the intense 20122013 dense water formation event in the
1435 northwestern mediterranean sea: Evaluation with an ensemble simulation approach, *Journal*
1436 *of Geophysical Research: Oceans*, 122(2), 1297–1324, doi:10.1002/2016JC012437.

1437 Xing, X., H. Claustre, S. Blain, F. d’Ortenzio, D. Antoine, J. Ras, and C. Guinet (2012), for
1438 in vivo chlorophyll fluorescence acquired by autonomous platforms: A case study with in-
1439 strumented elephant seals in the Kerguelen region (Southern Ocean, *Limnol. Oceanogr.*, pp.
1440 483–495, doi:10.4319/lom.2012.10.483.